NASA CONTRACTOR REPORT

NASA CR-1803

DESIGN AND EXPERIMENTAL RESULTS OF A HIGHLY LOADED, LOW SOLIDITY TANDEM ROTOR

by James L. Bettner

Prepared by
GENERAL MOTORS CORPORATION
Indianapolis, Ind. 46206
for Langley Research Center

NATIONAL AERONAUTICS AND SPACE ADMINISTRATION • WASHINGTON, D. C. • APRIL 1971

1. Report No.	2. Government Accession No.	3. Recipient's Catalog No.
NASA CR-1803		

4. Title and Subtitle	5. Report Date
DESIGN AND EXPERIMENTAL RESULTS OF A HIGHLY LOADED, LOW SOLIDITY TANDEM ROTOR	April 1971
	6. Performing Organization Code

7. Author(s)	8. Performing Organization Report No.
James L. Bettner	EDR 6627
	10. Work Unit No.

9. Performing Organization Name and Address	11. Contract or Grant No.
General Motors Corporation Indianapolis, Indiana 46206	NAS 3-11164
	13. Type of Report and Period Covered
12. Sponsoring Agency Name and Address	Contractor Report
National Aeronautics and Space Administration Washington, D.C. 20546	14. Sponsoring Agency Code

15. Supplementary Notes

16. Abstract

The overall performance of a single-stage turbine with a low solidity tandem rotor blade assembly was tested over a range of equivalent speeds and expansion ratios. The rotor blades were designed with negative hub reaction and a mean-line axial chord solidity of 1.092. The results of this investigation are compared with the performance of a modified tandem rotor blade which was designed to similar velocity diagrams but with a mean-section axial chord solidity of 1.852. Both rotors were tested with the same stator.

17. Key Words (Suggested by Author(s))	18. Distribution Statement
Turbines Cascade sectors Turbine blades Highly loaded blades	Unclassified - unlimited

19. Security Classif. (of this report)	20. Security Classif. (of this page)	21. No. of Pages	22. Price*
Unclassified	Unclassified	68	$3.00

*For sale by the National Technical Information Service, Springfield, Virginia 22151

FOREWORD

The research described in this report was conducted by the Allison Division of the General Motors Corporation under NASA contract NAS 3-11164 with Richard J. Roelke of the Lewis Research Center Fluid System Components Division as the NASA Project Manager. The report was originally issued as Allison report EDR 6627.

TABLE OF CONTENTS

LIST OF TABLES

LIST OF ILLUSTRATIONS

DESIGN AND EXPERIMENTAL RESULTS OF A HIGHLY LOADED, LOW SOLIDITY TANDEM ROTOR

By

J. L. Bettner

Detroit Diesel Allison Division, General Motors

SUMMARY

The overall performance of a single-stage turbine with a low solidity tandem rotor blade assembly was tested over a range of equivalent speeds and expansion ratios. The rotor blades were designed with negative hub reaction and a mean-line axial chord solidity of 1.092. The results of this investigation are compared with the performance of a modified tandem rotor blade which was designed to similar velocity diagrams but with a mean-section axial chord solidity of 1.852. Both rotors were tested with the same stator.

To expansion ratios of between 1.7 and 1.8, the total-to-total efficiency of the low solidity tandem rotor was essentially equivalent to that of the high solidity tandem rotor. The total efficiency of the low solidity tandem turbine was 86.4% at design equivalent speed—4660 rpm (487.99 rad/sec)— and expansion ratio—P_{t_o}/P_{t_3} = 2.01. This is three points lower than the modified higher solidity tandem blade rotor design point efficiency. The maximum efficiency of the low solidity tandem blade was 90.6%.

The low solidity tandem blade developed negative hub reaction, but not quite to the degree as did the modified higher solidity tandem turbine. Negative reaction existed at the hub for the low solidity tandem blade up to expansion ratios of 2.16. Beyond this expansion ratio, the reaction was positive.

Rotor exit surveys of total pressure, total temperature, and gas angle showed that the decrease in the overall total-to-total efficiency, relative to the higher solidity modified tandem blade, was primarily due to a high loss generated by probable suction surface flow separation in the tip region of the blade.

INTRODUCTION

The NASA Lewis Research Center has initiated a series of experimental investigations of several advanced turbine blade concepts designed to substantially increase the blade loading while maintaining high levels of efficiency. One of these concepts is a tandem rotor blade which has two staggered airfoils on a common base (Figure 12). The theory of the tandem blade is to distribute the aerodynamic loading between two airfoils and begin the diffusion process on the aft airfoil with a thin boundary layer.

The design of the first tandem blade of this series is presented in Reference 1 and the test results, including a comparison with a reference plain blade, were reported in Reference 2. Comparison of these two blades showed that the tandem blade had somewhat higher efficiency at rotor speeds above design speed but fell off in efficiency at design and lower speeds. At design speed and pressure ratio, the tandem blade turbine total efficiency was 87.6% and the plain blade turbine total efficiency was 88.4%. Subsequent cascade and rotor tests (References 3 and 4) of the same tandem blade but with a modified aft airfoil showed significant performance improvement. The modified tandem blade turbine had higher efficiency than the original tandem blade for almost all of the operating conditions investigated, including a gain of 1.8 points in total efficiency at the design speed and pressure ratio.

In view of these positive results for the tandem blade, it was decided to design and test a second tandem blade having a much lower solidity. The mean-section solidity of the first tandem blade was 1.852 and the solidity selected for the second tandem blade, herein referred to as the low solidity tandem, was 1.092. This report presents the design and test results of the low solidity tandem blade.

The low solidity tandem rotor was tested in the same single-stage test rig previously used in this test series. Performance data were taken from 70 to 110% of design equivalent speed over a range of expansion ratios from 1.4 to 2.6. Rotor exit surveys were conducted at the design equivalent speed and expansion ratio. Circumferential traverses with a combination total pressure, temperature, and yaw angle probe were made at constant radii to map the flow characteristics at the rotor trailing edge. The test results are compared with the modified tandem performance results.

All testing was conducted while operating the test rig with inlet conditions of approximately 2.7 atmospheres absolute pressure and 650°R (361°K) temperature.

SYMBOLS

C_x	Axial chord, in. (cm)
H_i	Incompressible shape factor
ΔH	Specific work output, Btu/lb (joule/kg)
$\dot{m}$	Mass flow rate, lb/sec (kg/sec)
N	Rotational speed, rpm (rad/sec)
P	Pressure, lb/in.^{2} (N/m^2)
P_{To}/P_{T3}	Total-to-total expansion ratio
d_t	Trailing edge diameter, in. (cm)
d_l	Leading edge diameter, in. (cm)
R	Reaction defined as $1 - (W_1^2/W_3^2)$
s	Blade spacing, in. (cm)
t	Throat dimension, in. (cm)
T	Temperature, °R (°K)
U	Blade tangential velocity, ft/sec (m/sec)
V	Absolute gas velocity, ft/sec (m/sec)
W	Relative gas velocity, ft/sec (m/sec)
X	Axial coordinate, in. (cm)
Y	Tangential coordinate, in. (cm)
α	Absolute gas angle measured from tangential, degrees
β	Relative gas angle measured from tangential, degrees
Γ	Torque, ft-lb (N-m)
γ	Ratio of specific heats

Δ Change of variable

δ Blade deflection, in. (cm)

δ_o Ratio of inlet air total pressure to standard sea level conditions

ϵ Function of γ defined as $\frac{\gamma^*}{\gamma} \frac{\left(\frac{\gamma+1}{2}\right)^{\gamma/(\gamma-1)}}{\left(\frac{\gamma^*+1}{2}\right)^{\gamma^*/(\gamma^*-1)}}$

η_T Adiabatic efficiency defined as the ratio of turbine work based on torque, weight flow, and speed measurements to the ideal work based on inlet total temperature, and inlet and outlet total pressure both defined as sum of static pressure plus pressure corresponding to the gas velocity.

η_t Adiabatic efficiency defined as the ratio of turbine work based on measured inlet and exit total temperature to ideal work based on measured inlet total temperature and pressure and measured exit total pressure.

θ_{cr} Squared ratio of critical velocity at turbine inlet temperature to critical velocity at standard sea level temperature.

ν Ratio of blade speed to isentropic gas velocity based on inlet total temperature and pressure and exit static pressure, U_m/V'

ρ Density, lb/ft^3 (kg/m^2)

σ_x Blade axial chord solidity defined as C_x/s

ψ_t Compressible tangential lift coefficient defined as

$$\frac{s}{C_x}\left(\frac{\rho_{st\ 3}\ V_{x3}\ \Delta V_{u1-3}}{P_{T1\ rel} - P_{st3}}\right)$$

Subscripts

o	Station at stator inlet (all stations are shown in Figure 2)
1	Station at free-stream conditions between stator and rotor
2	Station at outlet of rotor just downstream of trailing edge
3	Station downstream of turbine
a	Aft airfoil
cr	Conditions at Mach number of unity
f	Forward airfoil
m	Mean section
rel	Relative to moving blade
st	Static
T	Total
T-T	Total-to-total
t	Tip section
u	Tangential direction
x	Axial direction

Superscript

'	Ideal or isentropic condition

BLADE DESIGN

AERODYNAMIC DESIGN

The objective of this program was to design and test a single-stage turbine rotor having very highly loaded, low solidity blades. This high loading was to be achieved without flow separation by utilizing tandem airfoils.

The test rig, including the stator blade row, used with the low solidity tandem rotor was developed in the program described in Reference 1. This unit has a 30-in. (76.2-cm) tip diameter and a constant hub-tip radius ratio of 0.7. The overall design point characteristics were:

- Equivalent specific work output, $\Delta H/\theta_{cr}$ — 20.0 Btu/lb (46.5×10^3 joules/kg)
- Equivalent weight flow, $(\dot{m}\sqrt{\theta}_{cr}\ \epsilon)/\delta_o$ — 47.7 lb/sec (21.6 kg/sec)
- Equivalent blade tip speed, $U_t/\sqrt{\theta}_{cr}$ — 610.0 ft/sec (186.1 m/sec)
- Pressure ratio, P_{To}/P_{T3} — 2.01
- Total efficiency, η_T — 88.7
- Exit swirl measured from tangential, α_3 — 90.0 degrees

Velocity Diagrams

During the course of the initial turbine rig test (Reference 5), the weight flow measured at design speed and pressure ratio was 47.7 lb/sec (21.7 kg/sec) instead of 45.51 lb/sec (20.6 kg/sec) as designed. Because of this, it was decided to develop new velocity diagrams for the tandem blades of the current investigation. The diagrams were developed using the following assumptions and information:

1. The measured stator throat and trailing edge dimensions were used.
2. The stator exit total pressure survey as determined in an earlier test (Reference 5) was used.
3. The assumption that all stator loss occurred downstream of the throat.

4. The assumption that the rotor efficiency was radially constant and equaled the average value of 92.2% as determined from an earlier tandem blade test (Reference 2).

These final diagrams, which are presented in Figure 1, satisfied all of the imposed constraints except for a small amount of exit whirl. The diagrams incorporate a considerable amount of negative hub reaction (R_h) defined as

$$R_h = 1 - \left(W_1^2 / W_3^2\right)_h \tag{1}$$

The radial variation of design blade reaction is:

	Hub	Mean	Tip
Reaction	-0.851	0.312	0.722

The definition of reaction used in Reference 1 was

$$R = \left(W_3 / W_1\right) - 1 \tag{2}$$

which resulted in a hub section design value of -0.25. When computed using Equation 1, the Reference 1 design hub reaction was -0.778. Measuring station nomenclature is shown in Figure 2.

Solidity and Aerodynamic Loading Considerations

The objective of this research program was to examine the performance of a highly loaded tandem airfoil. High loading is synonymous with large values of tangential lift coefficient (ψ_t) which is essentially a compressible form of Zewifel's (Reference 6) actual-to-ideal loading coefficient and defined as

$$\psi_t = \frac{s}{C_x}\left(\frac{\rho_{st3}\ V_{x3}\ \Delta V_{u1\text{-}3}}{P_{T1\ rel} - P_{st_3}}\right) \tag{3}$$

The experimental results of References 7 and 8 have shown that low solidity tandem blades with large design values of lift coefficient can maintain high levels of performance. Based on the velocity diagrams, a hub axial chord of 2.2 in. (5.59 cm) and 50 blades, the hub section ψ_t value was 1.131. The axial chord was then tapered radially to produce mean and tip section ψ_t values of 1.200 and 1.232, respectively. The corresponding hub, mean, and tip section values of axial chord solidity were 1.667, 1.092, and 0.690, respectively. These data, along with other design data, are presented in Table I. The design values of ψ_t are compared in Table II with those of the tandem stator of Reference 7 and the tandem rotor of Reference 4.

Airfoil Design

Hub, mean, and tip section throat velocity diagrams were computed by an iterative calculation procedure which satisfies continuity (including trailing edge blockage) and conserves tangential momentum on a stream sheet for a straight-back blade. A trailing edge diameter of 0.030 in. (0.0762 cm) was used in the calculation. When the throat velocity diagrams were determined, the throat dimension was calculated from

$$t = \left(s \sin \beta_1\right) - d_{ta} \tag{4}$$

The resulting radial distribution of throat dimension is included in Table I.

The blade section profile shapes were determined by iterating with the radial section geometry until satisfactory surface velocity distributions were achieved. The surface velocities were computed by the two-dimensional, compressible flow methods described in References 9 and 10. Variations of streamtube thickness were accounted for in the axial direction. Hub, mean, and tip section total temperature, total pressure, flow, and gas angle input data were supplied from the velocity diagrams of Figure 1.

Both aerodynamic and mechanical constraints were imposed on the blade profile design. The foremost constraint was that flow separation was to be eliminated from the suction surface. If this was not possible, then separation was to be delayed as far as possible into the trailing edge region. Attainment of no flow separation on the blading surfaces was to be achieved by:

1. Loading the forward and aft airfoils equally (If equal amounts of lift are generated by both the forward and aft airfoils, then the opportunity exists to keep the required surface velocity diffusion low on each airfoil, preventing flow separation.)

2. Keeping the velocity levels on the pressure surface as low as possible (This would help to avoid unnecessary high velocity levels on the suction surface.)

3. Avoiding velocity spikes and large decelerations on the suction surface

4. Having a converging slot between blades

The forward and aft airfoils were located so that an overlap region of approximately 15% of the axial chord occurred at about the midpoint of the overall axial chord. Further, the trailing edge of the forward airfoil was located circumferentially so that it divided the area between two adjacent tandem blades into about 30% for the slot flow and 70% for the mainchannel flow. These features are illustrated in Figure 3.

Preliminary hub, mean, and tip sections were constructed which satisfied the previously discussed geometric constraints. An iteration on the amount of flow split between the slot and mainchannel was continued until the velocities computed on the pressure surface of the forward airfoil at the trailing edge matched those on the suction surface at the trailing edge of the same airfoil. The magnified computation procedure of Reference 10 was incorporated to examine the details of the forward airfoil trailing edge flow. When the flow split ratio was determined, the airfoil shapes were then iterated on until satisfactory surface velocity distributions around both airfoils were obtained. The magnifier calculation procedure was also used to determine the aft airfoil trailing edge region geometry. The position and shape of the trailing edge geometry was iterated on until the velocities computed on the pressure and suction surfaces at the trailing edge were equal. The resulting hub, mean, and tip section profiles are presented in Figures 4, 5, and 6 with the respective surface critical velocity ratio distributions shown in Figures 7, 8, and 9. Blade section coordinates are listed in Table III.

The effect of the free-stream static pressure distribution on the behavior of the suction surface boundary layer was investigated by using the calculation technique of Truckenbrodt (Reference 11). This calculation procedure is discussed in Appendix A. Flow separation was assumed to occur when the incompressible shape factor (H_i) attains values between 1.8 to 2.2. The Truckenbrodt calculation scheme has been shown to be basically a conservative prediction method---i.e., flow fields tend to be more tolerant to adverse pressure gradient effects than the Truckenbrodt approach would indicate. Because of this, the flow separation criterion of $H_i = 2.2$ was selected in this tandem blade design. The calculated values of H_i at the hub, mean, and tip sections for both the forward and aft airfoils are shown in Figure 10. The surface locations where H_i equals 2.2 are indicated in Figures 7, 8, and 9. It can be seen from the boundary layer data (Figure 10) that some flow separation ($H_i > 2.2$) is expected to occur on the blading surfaces. Even though flow separation may occur, the separation region would be located far enough into the trailing edge region that most of the gas turning would already be accomplished and the design velocity diagrams would essentially be achieved.

MECHANICAL DESIGN

Stress and Deflection Analysis

A stress and deflection analysis was made of the blade geometry with the design operating point flow conditions. Axial and tangential forces acting on both the forward and aft blades are presented in Table IV. These forces were determined from the surface static pressure distributions calculated about the airfoils at the design operating point. The blades were investment cast from Inco 718 material.

An investigation was conducted to determine the blade stacking axis that would (1) keep the blade stresses under the maximum allowable levels and (2) maintain the slot dimension to within 0.005 in. (0.0127 cm) of design value at the design operating condition. Stacking the blade to have a nearly radial aft airfoil trailing edge satisfied the slot dimension criteria and was therefore selected. The stacked blade, showing the relative locations of the section centers of gravity, is presented in Figure 11. The blade stresses and deflections are listed in Table V. Figure 12 shows the full rotor wheel assembly.

Blade Dynamic and Flutter Analyses

Figure 13 presents the vibrational characteristics of the tandem blade forward and aft airfoils. These results show that several modes of blade vibration could be excited by the test rig engine orders in the turbine operating speed range. Testing, however, showed that the mechanical characteristics of the blades were such that the excitation was sufficiently damped out at most operating points. Excessive vibrational stress was encountered, however, at low speeds and high expansion ratios.

The blade flutter was also considered during the mechanical design of the blade. The prime variables which affect blade flutter are (1) the angle (i.e., incidence) at which the fluid particles strike the blade leading edge region and (2) their kinetic energy. Figures 14 and 15 present the envelope of incidence-relative velocity to which both airfoils are subjected. The flutter boundaries were predicted to lie at large distances---approximately W = 3800 ft/sec (1178 m/sec)---to the right of Figures 14 and 15. These results indicate, along with experimental confirmation, that both the forward and aft airfoils were very stable in both stalled and unstalled flutter.

APPARATUS AND INSTRUMENTATION

The apparatus used in this investigation is described in Reference 1 and consisted of a single-stage cold air turbine test rig, suitable housings to provide uniform inlet flow conditions, and a dynamometer to absorb and measure the turbine power output. A schematic of the test rig and air supply facility is shown in Figure 16. Air is supplied at approximately 3-atmospheres pressure and a temperature of approximately 700°R (388.5°K). The inlet pressure is controlled by the separate air compressor supply and/or by a throttle valve in the inlet supply line. The turbine expansion ratio is controlled by a throttle valve in the exhaust system duct.

The turbine test rig instrumentation is also described in detail in Reference 1. The airflow is measured using a Bailey adjustable orifice which is calibrated with an ASME flow nozzle. The turbine power output is absorbed by two Dynamatic dry-gap eddy current brakes. The torque of each dynamometer is measured separately by a dual output strain gage load cell connected in tension to the dynamometer torque arm.

Measurements of total temperature and total pressure were made at stations 0 and 3 (Figure 2). Turbine inlet temperature was measured with 20 iron-constantan thermocouples arranged five to a rake. The sensing elements were located on centers of equal annular areas, and the rakes were spaced 90 degrees apart. Four Kiel-type total pressure probes, also located at the inlet, were used to establish the desired inlet total pressure. The turbine exit measuring station (station 3) was instrumented with five combination total pressure, total temperature, self-aligning flow angle probes. The sensing elements of the five combination probes were located at the center of five equal annular areas.

Static pressures were measured with four taps on both the inner and outer walls located around the annulus at stations 0, 1, 2, and 3. The stator outlet (station 1) static pressure taps were centrally located on the projected stator flow passage.

A rotor exit survey was performed approximately 0.125 in. (0.318 cm) downstream of the rotor blade trailing edge (station 2). Total pressure, total temperature, and flow angle were measured at seven radii from hub to tip for a circumferential arc of 22 degrees. The measurements were taken concurrently with a single combination probe.

CALCULATION PROCEDURE

OVERALL TURBINE PERFORMANCE

The turbine performance was rated on the basis of two expansion ratios defined as (1) the ratio of the inlet total pressure to rotor discharge static pressure and (2) the ratio of inlet total pressure and rotor exit total pressure. The inlet total pressure at station o was calculated from continuity using the average of the 20 measured total temperatures, the average of the hub and tip static pressures, the mass flow rate, and the inlet annulus area. The flow was assumed to be axial. The exit total pressure at station 3 was also calculated from continuity using the mass flow rate, the annulus area, the average of the hub and tip static pressures, the average flow angle, and the total temperature. The total temperature was calculated from the enthalpy drop which, in turn, was based on the measured airflow, torque, and speed.

The efficiencies were calculated as a ratio of the actual enthalpy drop as obtained from torque, mass flow rate, and rotor speed measurements to the ideal enthalpy drop as obtained from the inlet total temperature and the associated calculated expansion ratio.

ROTOR EXIT SURVEY

The performance of the turbine as described by a rotor exit survey at the design point condition is based on measured expansion ratio, inlet temperature, and exit temperature. The measured expansion ratio is based on the average total pressure indicated by the four inlet Kiel probes and the exit total pressure measured by the survey probe. The inlet total temperature is the average temperature of the 20 inlet thermocouples; the exit total temperature is measured by the thermocouple on the survey probe. These thermocouples were corrected for Mach number based on a linear variation of hub and tip static pressure and the measured total pressure. The isentropic work of the turbine is based on the measured inlet temperature and measured total pressure ratio. The actual work is the difference of the enthalpies associated with the measured inlet and exit temperatures. The efficiency at each station in the survey is the ratio of the actual work to the isentropic work.

The measured absolute flow angle and an assumed linear variation of static pressure from hub to tip were used to determine the velocity diagrams at the rotor exit.

EXPERIMENTAL RESULTS

TURBINE OVERALL PERFORMANCE

The low solidity tandem rotor was tested in the same single-stage rig used to test the modified tandem blade reported in reference 4. The performance of the low solidity tandem rotor will be compared with that of the modified tandem blade. Figure 17 presents the modified tandem rotor assembly which may be compared with the low solidity design shown in Figure 12. The solidity of the modified tandem blade is about 1.7 times that of the low solidity tandem blade. Performance data were taken from 70 to 110% of design equivalent speed over a range of expansion ratios from 1.4 to 2.6. Rotor exit surveys were conducted at the design equialent speed and expansion ratio. Circumferential traverses with a combination total pressure, temperature, and yaw angle probe were made at constant radii to map the flow characteristics at the rotor trailing edge.

The overall performance of the low solidity tandem rotor turbine and the modified tandem turbine are shown in Figures 18 and 19, respectively. These maps present the equivalent shaft work ($\Delta H/\theta_{cr}$) as a function of the equivalent flow-speed parameter ($\dot{m}N\,\epsilon/60\,\delta_o$) for lines of constant total-to-total expansion ratio, P_{To}/P_{T3}, and equivalent rotor speed ($N/\sqrt{\theta}_{cr}$). Contours of constant total efficiency (η_T) are also included. The total efficiency of the low solidity tandem turbine obtained at design work and speed was 85.4%. This compares with a value of about 89.6% in Figure 19 for the modified tandem blade. Also, the low solidity tandem rotor does not exhibit the broad islands of high efficiency as did the modified tandem turbine. It does, however, resemble the modified tandem characteristics at the lower speeds and lower expansion ratios.

The variation of equivalent flow is shown in Figure 20 as a function of total-to-total expansion ratio and equivalent speed. The low solidity tandem turbine choked at an expansion ratio of about 2.2. Figure 7 of Reference 4 shows that the modified tandem turbine choked flow was 48 lb/sec (21.8 kg/sec) at an expansion ratio of about 2.0. At design speed and expansion ratio, the design flow of the low solidity tandem was 47.7 lb/sec (21.7 kg/sec) which agreed with that measured.

Figure 21 illustrates the variation of equivalent torque ($\Gamma\,\epsilon/\delta_o$) with total-to-total expansion ratio and equivalent speed. These torque characteristics indicate that limiting loading had not yet been reached but, at the high values of expansion ratio, limiting loading was being approached. At design speed and expansion ratio, the measured value of equivalent torque was 1485 ft-lb (2013 N-m) compared to the design value of 1520 ft-lb (2060 N-m). Operation at low equivalent speed and high values of expansion was prevented because of high vibrational blade stress.

The variation of equivalent work ($\Delta H/\theta_{cr}$) with equivalent speed and expansion ratio is shown in Figure 22. These results indicate that, at design expansion ratio and speed, the turbine equivalent work output was 19.5 Btu/lb (45.4×10^3 joules/kg) compared to the design value of 20.0 Btu/lb (46.6×10^3 joules/kg).

Figure 23 presents the total-to-total efficiency as a function of blade-jet speed ratio ($\nu = U_m/V'$). V' is the exit ideal spouting velocity based on inlet total pressure and temperature and exit static pressure. At the design value of $\nu = 0.446$, the efficiency was 86.4%. The design value of efficiency was 88.7%. The peak measured efficiency was 90.6% occurring at a blade-jet speed ratio of about 0.55.

A comparison of static pressure distribution through the low solidity and modified tandem turbines is shown in Figure 24. Design point values of total-to-total expansion ratio (P_{T_O}/P_{T3}) are included in Figure 24 and reflect, primarily, differences in assumed values of efficiency and flow rate used in the development of the velocity diagrams for the two turbines. The design point values of P_{T_O}/P_{T3} were 2.01 and 2.10 for the low solidity and modified tandem blade turbines, respectively. Design values of efficiency and flow rate were 84% and 45.51 lb/sec (20.6 kg/sec) for the modified tandem and 88.7% and 47.7 lb/sec (21.7 kg/sec) for the low solidity tandem blade turbine.

The static pressure distribution shown in Figure 24, in particular at the stator exit, is quite different for the two turbines. Below expansion ratios of about 1.9, the stator exit hub and tip static pressure is similar in shape but of a different level for the two turbines. Above expansion ratios of about 1.9, the static pressure differs both in shape and level for the two turbines. The variation of static pressure in these two regions of expansion ratio is discussed in the following paragraphs.

Stator Exit Static Pressure for $P_{T_O}/P_{T3} < 1.9$

Figure 24 shows that up to $P_{T_O}/P_{T3} \sim 1.9$ the modified tandem stator exit static pressure was similar in shape but of lower value than for the low solidity tandem. The modified tandem blade had about 3% more throat area than the low solidity tandem blade. This is a consequence of the assumption of efficiency and flow rate used in the development of the velocity diagrams for the two turbines. For the same expansion ratio across the two turbines, the low solidity tandem had more reaction across the rotor and less reaction across the stator (i.e., higher stator exit static pressure) than did the modified tandem turbine.

Stator exit static pressure for $P_{T_o}/P_{T3} > 1.9$

Beyond expansion ratios of 1.9, the stator exit static pressure variation changed substantially in both level and shape (particularly in the hub region) with expansion ratio for the two turbines. In the tip region, the stator exit static pressure variation was similar in shape but of a different level for all values of P_{T_o}/P_{T3} for the two turbines. This is the consequence of having different rotor throat areas. However, in the hub region, the low solidity tandem blade changed from negative to positive reaction at an expansion ratio of 2.16 while the modified tandem continued to exhibit negative hub reaction characteristics up to expansion ratios of 2.47. The low solidity tandem blade developed less than design negative hub reaction while the modified tandem developed greater than its design amount of negative hub reaction at the respective design expansion ratios of 2.01 and 2.10. This decrease in negative hub reaction of the low solidity tandem blade was probably due to an increase in rotor loss with a subsequent increase in the rotor expansion ratio.

TURBINE ROTOR EXIT SURVEY

Circumferential traverses with a combination total pressure, temperature, and yaw angle probe were made at constant radii to map the flow characteristics at the rotor trailing edge. These surveys yield the circumferential variation of temperature ratio $(T_{T_o} - T_{T2})/T_{T_o}$, total pressure ratio, P_{T_o}/P_{T2}, blade exit absolute flow angle, and local efficiency. Typical examples of these surveys in approximately the midspan region of the blade are shown in Figures 25 through 28. From this survey, contour maps of temperature ratio, pressure ratio, and local total-to-total efficiency were constructed and are presented in Figures 29 through 31. The total temperature ratio contour map of Figure 29 shows the changes in work extraction from the fluid over the annulus sector surveyed. Most of the energy was extracted from the fluid in the lower two-thirds of annulus. Very little energy was extracted from the fluid at the tip section.

Figure 30 illustrates that the stage total pressure (P_{T_o}/P_{T2}) was quite uniform over the whole annulus, except near the hub wall where it increased slightly. The wake of the stator is somewhat evident in this illustration.

The efficiency contour map is presented in Figure 31. The highest values of efficiency occurred in the middle third of the passage annulus. The values of efficiency ranged from broad islands of 90% to very small islands of above 94%. The lower third of the annulus exhibited efficiencies that ranged from 90 to 80% with small islands at the hub wall of 76%. The losses were the highest in the tip region. The upper third of the annulus experienced efficiencies that ranged from 90% at about the two third span but which progressively fell to below 68% at the tip wall.

Graphic integration of the traces of efficiency at constant radii yielded a plot of the circumferentially averaged efficiency at station 2 as a function of radius. The radial variation of this average efficiency for both the low solidity tandem blade and the modified tandem blade is shown in Figure 32. Comparison of these two turbines shows that the low solidity tandem turbine had significantly lower efficiency in the tip region (ranging from 4 to 14 points lower) than the modified tandem turbine. In the mean section region, the low solidity tandem turbine efficiency was still lower than the modified tandem turbine but by only about two points. The low solidity tandem turbine, however, had a higher efficiency in the lower third of the annulus.

The tandem rotor blade of the current investigation was designed with low solidity with the resulting large values of tangential lift coefficient. The solidity was lowest ($\sigma_x = 0.69$) and the loading was highest ($\psi_t = 1.232$) at the tip section. During the blade design, effort was made to keep the suction surface velocities as low as possible (preferably subsonic) and to minimize the flow decelerations. A later analysis indicated that larger than design maximum suction surface velocities (i.e., $W/W_{cr} \sim 1.2$) and flow decelerations may have occurred on the aft airfoil. These flow conditions may have resulted in the formation of a normal shock standing on the secondary airfoil suction surface. The potential for a normal shock and the increased diffusion may have triggered boundary layer separation from the airfoil suction surface, resulting in the high loss experimentally obtained in the tip region. This premise is reinforced by the fact that the performance deteriorated rapidly (Figure 18) with increasing expansion ratio on a given speed line. Increasing the expansion ratio across the turbine results in larger velocity levels on the blading surfaces and an increased possibility of flow separation. Separated flow in the tip region would cause a flow shift towards the hub with an accompanying flow acceleration in that region. This would explain the decrease in the measured amount of negative hub reaction.

SUMMARY OF RESULTS

The overall performance of a single-stage turbine incorporating low solidity tandem airfoils was investigated over a range of equivalent speeds and expansion ratios. The performance was compared with a high solidity tandem blade turbine. The mean-section solidities of the two turbines were 1.092 and 1.853, respectively. Both tandem rotor blade configurations were designed to similar velocity diagrams which incorporated negative hub reaction. Both tandem blade turbines were tested with the same stator. The following results were obtained.

1. Up to expansion ratios of between 1.7 and 1.8, the total-to-total efficiency of the low solidity tandem rotor was essentially equivalent to that of the high solidity tandem blade rotor. However, the low solidity tandem blade became progressively less efficient, when compared to the modified tandem blade, as the expansion ratio was increased to larger values. The maximum efficiency measured for the low solidity tandem blade was 90.6%.

2. The total efficiency of the subject tandem turbine was 86.4% at design equivalent speed and expansion ratio. This is three points lower than the high solidity modified tandem blade turbine.

3. A survey taken at the rotor trailing edge showed that the low solidity tandem blade had much higher losses in the upper third of the blade. However, in the hub region, the efficiency of the low solidity tandem blade was slightly higher than the high solidity tandem blade.

4. The choked level of equivalent flow was essentially the same for both the low solidity and modified tandem blade turbines. However, the modified tandem blade turbine choked at a lower expansion ratio ($P_{T_O}/P_{T3} \sim 2.0$) than did the current low solidity turbine ($P_{T_O}/P_{T3} \sim 2.2$).

5. The low solidity tandem rotor had negative hub reaction at the design pressure ratio; however, it was less than the design value and less than the high solidity modified tandem blade turbine. The differences in pressure distribution through the blading of the two turbines were small at low pressure ratios but became more pronounced at higher pressure ratios.

6. It is suspected that significantly larger than design values of velocity and diffusion occurred in the tip region of the airfoil on the suction surface. These conditions probably promoted flow separation from the aft airfoil and a subsequent flow shift toward the hub region with resulting high losses at the blade tip and a generally higher rotor reaction.

REFERENCES

1. Lueders, H. G. Experimental Investigation of Advanced Concepts to Increase Turbine Blade Loading, Vol I. Analysis and Design. NASA CR-735. June 1967.

2. Lueders, H. G. Experimental Investigation of Advanced Concepts to Increase Turbine Blade Loading, Vol III. Performance Evaluation of Tandem Rotor Blade. NASA CR-1254. December 1968.

3. Nosek, S. M. and Kline, J. F. Two-Dimensional Cascade Investigation of a Turbine Tandem Blade Design. NASA TMX-1836. July 1969.

4. Lueders, H. G. Experimental Investigation of Advanced Concepts to Increase Turbine Blade Loading, Vol VI. Performance Evaluation of Modified Tandem Rotor Blade. NASA CR-1616. June 1970.

5. Lueders, H. G. Experimental Investigation of Advanced Concepts to Increase Turbine Blade Loading. Vol II., Performance Evaluation of Plain Rotor Blade. NASA CR-1172. August 1968.

6. Zweifel, O. "The Spacing of Turbo-Machine Blading, Especially with Large Angular Deflection." Brown Bovevi Review. Vol 32 (December 1945), pp. 436-444.

7. Bettner, J. L. Experimental Investigation in an Annular Cascade Sector of Highly Loaded Turbine Stator Blading, Vol III. Performance of Tandem Blade. NASA CR-1341. May 1969.

8. Bettner, J. L. and S. M. Nosek. "Summary of Tests on Two Highly Loaded Turbine Blade Concepts in Three Dimensional Cascade Sector." ASME Paper 69-WA/GT-5.

9. Katsanis, T. and McNally, W. D. FORTRAN Program for Calculating Velocities and Streamlines on a Blade-to-Blade Stream Surface of a Tandem Blade Turbomachine. NASA TN-D-5044 (1969).

10. Katsanis, T. and McNally, W. D. FORTRAN Program for Calculating Velocities in a Magnified Region on a Blade-To-Blade Stream Surface of a Turbomachine. NASA TN-D-5091 (1969).

11. Truckenbrodt, E. A Method of Quadrature for Calculation of Laminar and Turbulent Boundary Layer in Case of Plane and Rotationally Symmetric Flow. NACA TM-1379 (1955).

12. Culick, F. E. C. and Hill, J. A. F. "A Turbulent Analog of the Stewartson-Illingworth Transformation." Journal of Aeronautical Sciences. Vol 25, No. 4 (April 1958), pp. 259-262.

13. Stewartson, K. "Correlated Compressible and Incompressible Boundary Layers." Proceedings of the Royal Society. Series A, Vol 200, No. A1060 (December 1949), pp. 84-100.

APPENDIX A

BOUNDARY LAYER ANALYSIS

A prediction of the growth rate of the blade surface boundary layer was required for determining the location of incipient flow separation. The momentum integral equations for the compressible, turbulent boundary layer along a two-dimensional or axisymmetric surface have been integrated and formulated into Allison computer program L42. The integral approach used was that of Culick and Hill (Reference 10) which uses the Stewartson-Illingworth (Reference 11) transformation to transform the compressible form of the momentum integral equation to a corresponding incompressible form. The turbulent boundary layer calculation procedure of Truckenbrodt (Reference 9) was applied to this incompressible form of the equations. The results of the boundary layer calculation procedure were then transformed back to the compressible flow field. Input data for this program consists of free-stream total pressure, free-stream total temperature, Mach number distribution, and surface geometry. The boundary layer calculation may begin at any point along the surface if initial values of momentum thickness and shape factor are known. Flow separation is said to occur when the incompressible boundary layer shape factor attains values between 1.8 and 2.2.

Table I.
Tandem rotor design data.

Parameter	Units	Hub	Mean	Tip
Axial chord, C_x	in. (cm)	2.200 (5.588)	1.750 (4.445)	1.300 (3.302)
Blade spacing, s	in. (cm)	1.319 (3.350)	1.602 (4.070)	1.885 (4.788)
Axial chord solidity, σ_x		1.667	1.092	0.690
Throat dimension, t	in. (cm)	0.9141 (2.322)	1.0176 (2.5847)	1.1219 (2.8496)
Forward airfoil leading edge diameter, d_{lf}	in. (cm)	0.044 (0.1118)	0.084 (0.2134)	0.124 (0.3150)
Aft airfoil leading edge diameter, d_{la}	in. (cm)	0.094 (0.239)	0.100 (0.254)	0.110 (0.2794)
Forward airfoil trailing edge diameter, d_{tf}	in. (cm)	0.030 (0.076)	0.030 (0.076)	0.030 (0.076)
Aft airfoil trailing edge diameter, d_{ta}	in. (cm)	0.030 (0.076)	0.030 (0.076)	0.030 (0.076)
Inlet critical velocity ratio, $W/W_{cr})_o$		0.785	0.622	0.427
Exit critical velocity ratio, $W/W_{cr})_3$		0.577	0.750	0.810
Compressible tangential lift coefficient, ψ_t		1.131	1.200	1.232
Blade row reaction, R		-0.851	+0.312	+0.722

Table II.
Tandem blade lift coefficient design values.

	Hub	Mean	Tip
Low solidity tandem rotor	1.131	1.200	1.232
Tandem stator (Reference 7)	1.093	1.193	1.224
Modified tandem rotor (Reference 4)	0.742	0.641	0.547

Table III.

Tandem rotor hub section coordinates.

(Forward airfoil)

X		Y		X		Y	
in.	cm	in.	cm	in.	cm	in.	cm
1.9861	5.0447	2.2542	5.7256	3.1380	7.9705	3.1067	7.8910
1.9865	5.0457	2.2582	5.7358	3.1254	7.9385	3.0919	8.1074
1.9976	5.0739	2.3160	5.8826	3.1015	7.8778	3.0884	7.8445
2.0135	5.1143	2.3859	6.0601	3.0778	7.8176	3.0844	7.8343
2.0307	5.1580	2.4464	6.2139	3.0541	7.7574	3.0798	7.8226
2.0537	5.2164	2.5107	6.3771	3.0189	7.6680	3.0711	7.8005
2.0830	5.2908	2.5750	6.5405	2.9838	7.5788	3.0608	7.7744
2.1238	5.3945	2.6482	6.7284	2.9489	7.4902	3.0485	7.7431
2.1656	5.5006	2.7136	6.8925	2.9143	7.4023	3.0346	7.7078
2.2083	5.6091	2.7727	7.0426	2.8798	7.3146	3.0197	7.6700
2.2518	5.7196	2.8263	7.1788	2.8342	7.1988	2.9967	7.6116
2.3069	5.8596	2.8858	7.3299	2.7891	7.0843	2.9685	7.5399
2.3633	6.0028	2.9362	7.4579	2.7445	6.9710	2.9370	7.4599
2.4202	6.1473	2.9817	7.5735	2.7003	6.8587	2.9017	7.3703
2.4896	6.3236	3.0285	7.6923	2.6567	6.7480	2.8624	7.2704
2.5594	6.5009	3.0713	7.8011	2.6026	6.6106	2.8100	7.1374
2.6182	6.6502	3.1023	7.8798	2.5382	6.4470	2.7431	6.9674
2.6657	6.7709	3.1233	7.9331	2.4744	6.2849	2.6723	6.7876
2.7136	6.8925	3.1412	7.9786	2.4214	6.1503	2.6127	6.6362
2.7619	7.0152	3.1549	8.0134	2.3682	6.0152	2.5540	6.4871
2.8108	7.1394	3.1642	8.0370	2.3149	5.8798	2.4974	6.3433
2.8601	7.2646	3.1696	8.0507	2.2720	5.7708	2.4536	6.2321
2.8975	7.3596	3.1707	8.0535	2.2291	5.6619	2.4108	6.1234
2.9352	7.4554	3.1693	8.0500	2.1860	5.5524	2.3697	6.0190
2.9732	7.5519	3.1647	8.0383	2.1427	5.4424	2.3311	5.9209
3.0116	7.6494	3.1576	8.0203	2.1099	5.3591	2.3041	5.8524
3.0502	7.7475	3.1483	7.9966	2.0824	5.2892	2.2822	5.7967
3.0761	7.8133	3.1406	7.9771	2.0605	5.2336	2.2652	5.7536
3.1024	7.8801	3.1309	7.9524	2.0384	5.1775	2.2489	5.7122
3.1286	7.9466	3.1206	7.9263	2.0219	5.1356	2.2370	5.6819

Table III (cont.)
Tandem rotor mean section coordinates.
(Forward airfoil)

X		Y		X		Y	
in.	cm	in.	cm	in.	cm	in.	cm
2.4135	6.1303	2.5829	6.5605	3.2322	8.2097	3.2349	8.2166
2.4141	6.1318	2.5906	6.5801	3.2187	8.1754	3.2200	8.1788
2.4188	6.1437	2.6161	6.6448	3.1986	8.1244	3.2182	8.1742
2.4256	6.1610	2.6488	6.7279	3.1790	8.0746	3.2154	8.1671
2.4330	6.1798	2.6801	6.8074	3.1595	8.1175	3.2121	8.1587
2.4425	6.2039	2.7191	6.9065	3.1311	7.9529	3.2057	8.1424
2.4551	6.2359	2.7634	7.0190	3.1036	7.8831	3.1978	8.1224
2.4734	6.2824	2.8193	7.1610	3.0764	7.8140	3.1888	8.0995
2.4935	6.3334	2.8712	7.2928	3.0498	7.7464	3.1786	8.0736
2.5160	6.3906	2.9184	7.4127	3.0237	7.6801	3.1673	8.0449
2.5399	6.4513	2.9625	7.5247	2.9900	7.5946	3.1502	8.0015
2.5717	6.5321	3.0134	7.6540	2.9575	7.5120	3.1304	7.9512
2.6058	6.6187	3.0597	7.7716	2.9262	7.4325	3.1080	7.8943
2.6421	6.7109	3.1012	7.8770	2.8963	7.3566	3.0828	7.8303
2.6888	6.8295	3.1445	7.9870	2.8678	7.2842	3.0546	7.7586
2.7381	6.9547	3.1821	8.0825	2.8341	7.1986	3.0150	7.6581
2.7818	7.0657	3.2082	8.1489	2.7970	7.1043	2.9609	7.5206
2.8182	7.1582	3.2259	8.1937	2.7610	7.0129	2.9043	7.3769
2.8556	7.2532	3.2412	8.2326	2.7307	6.9359	2.8579	7.2590
2.8949	7.3536	3.2528	8.2621	2.7000	6.8580	2.8124	7.1434
2.9356	7.4564	3.2614	8.2839	2.6683	6.7774	2.7689	7.0330
2.9774	7.5625	3.2676	8.2997	2.6421	6.7109	2.7357	6.9486
3.0095	7.6441	3.2707	8.3075	2.6153	6.6428	2.7041	6.8684
3.0424	7.7276	3.2721	8.3111	2.5883	6.5742	2.6728	6.7889
3.0762	7.8135	3.2718	8.3103	2.5613	6.5057	2.6415	6.7094
3.1109	7.9016	3.2691	8.3035	2.5411	6.4543	2.6181	6.6499
3.1467	7.9926	3.2646	8.2920	2.5242	6.4114	2.5983	6.5996
3.1710	8.0543	3.2606	8.2819	2.5108	6.3774	2.5826	6.5598
3.1958	8.1173	3.2556	8.2692	2.4972	6.3428	2.5672	6.5206
3.2211	8.1815	3.2493	8.2532	2.4871	6.3172	2.5553	6.4904

Table III (cont.)
Tandem rotor tip section coordinates.
(Forward airfoil)

X		Y		X		Y	
in.	cm	in.	cm	in.	cm	in.	cm
2.5369	6.4437	3.0981	7.8691	3.2191	8.1765	3.5277	8.9603
2.5410	6.4541	3.0761	7.8131	3.2103	8.1541	3.5141	8.9258
2.5338	6.4358	3.0984	7.8699	3.1952	8.1158	3.5074	8.9087
2.5298	6.4256	3.1153	7.9128	3.1799	8.0769	3.5009	8.8922
2.5265	6.4173	3.1472	7.9938	3.1648	8.0385	3.4943	8.8755
2.5278	6.4206	3.1725	8.0581	3.1422	7.9811	3.4843	8.8501
2.5329	6.4335	3.1997	8.1272	3.1199	7.9245	3.4739	8.8237
2.5430	6.4592	3.2331	8.2120	3.0981	7.8691	3.4633	8.7967
2.5559	6.4919	3.2639	8.2903	3.0764	7.8140	3.4525	8.7693
2.5715	6.5316	3.2923	8.3624	3.0551	7.7599	3.4413	8.7409
2.5894	6.5770	3.3187	8.4294	3.0270	7.6885	3.4262	8.7025
2.6142	6.6400	3.3495	8.5077	2.9995	7.6187	3.4105	8.6626
2.6413	6.7089	3.3783	8.5808	2.9731	7.5516	3.3939	8.6205
2.6702	6.7823	3.4054	8.6497	2.9475	7.4866	3.3765	8.5763
2.7070	6.8757	3.4361	8.7276	2.9227	7.4236	3.3585	8.5305
2.7464	6.9758	3.4645	8.7998	2.8927	7.3474	3.3350	8.4709
2.7815	7.0650	3.4862	8.8549	2.8591	7.2621	3.3048	8.3941
2.8109	7.1396	3.5023	8.8958	2.8267	7.1798	3.2734	8.3144
2.8422	7.2191	3.5169	8.9329	2.8014	7.1155	3.2459	8.2445
2.8749	7.3017	3.5301	8.9664	2.7776	7.0551	3.2169	8.1709
2.9100	7.3914	3.5413	8.9949	2.7555	6.9989	3.1865	8.0937
2.9481	7.4881	3.5498	9.0164	2.7387	6.9562	3.1613	8.0297
2.9782	7.5646	3.5548	9.0291	2.7219	6.9136	3.1362	7.9659
3.0100	7.6454	3.5584	9.0383	2.7044	6.8691	3.1117	7.9037
3.0430	7.7292	3.5609	9.0446	2.6854	6.8209	3.0886	7.8450
3.0784	7.8191	3.5611	9.0451	2.6698	6.7812	3.0724	7.8038
3.1175	7.9184	3.5582	9.0378	2.6556	6.7452	3.0600	7.7724
3.1462	7.9913	3.5541	9.0274	2.6433	6.7189	3.0508	7.7490
3.1763	8.0678	3.5486	9.0134	2.6296	6.6791	3.0429	7.7289
3.2072	8.1458	3.5424	8.9976	2.6173	6.6479	3.0388	7.7185

Table III (cont.)
Tandem rotor hub section coordinates.
(Aft airfoil)

X		Y		X		Y	
in.	cm	in.	cm	in.	cm	in.	cm
2.9430	7.4752	2.6472	6.7238	4.1976	10.6619	2.2542	5.7256
2.9512	7.4960	2.6737	6.7911	4.1740	10.6019	2.2419	5.6944
2.9718	7.5483	2.6996	6.8569	4.1550	10.5537	2.2553	5.7284
2.9932	7.6027	2.7204	6.9098	4.1362	10.5859	2.2680	5.7607
3.0259	7.6857	2.7458	6.9743	4.1112	10.4424	2.2845	5.8026
3.0705	7.7990	2.7715	7.0396	4.0862	10.3789	2.3005	5.8432
3.1164	7.9156	2.7875	7.0802	4.0488	10.2839	2.3230	5.9004
3.1629	8.0337	2.7972	7.1048	4.0116	10.1894	2.3436	5.9527
3.2101	8.1536	2.8027	7.1188	3.9747	10.0953	2.3624	6.0004
3.2578	8.2748	2.8044	7.1231	3.9380	10.0025	2.3796	6.0441
3.3057	8.3964	2.8029	7.1193	3.8893	9.8788	2.3998	6.0954
3.3542	8.5196	2.7978	7.1064	3.8409	9.7558	2.4171	6.1394
3.4029	8.6433	2.7897	7.0858	3.7928	9.6337	2.4328	6.1793
3.4645	8.7998	2.7755	7.0497	3.7447	9.5115	2.4477	6.2171
3.5390	8.9890	2.7526	6.9916	3.6968	9.3898	2.4603	6.2491
3.6139	9.1793	2.7260	6.9240	3.6373	9.2387	2.4739	6.2837
3.6767	9.3388	2.7008	6.8600	3.5661	9.0578	2.4884	6.3205
3.7273	9.4673	2.6775	6.8008	3.4951	8.8775	2.5014	6.3535
3.7783	9.5968	2.6513	6.7343	3.4360	8.7274	2.5119	6.3802
3.8295	9.7269	2.6232	6.6629	3.3886	8.6070	2.5195	6.3995
3.8810	9.8577	2.5921	6.5839	3.3414	8.4871	2.5266	6.4175
3.9333	9.9905	2.5554	6.4907	3.2943	8.3675	2.5338	6.4358
3.9729	10.0911	2.5238	6.4104	3.2469	8.2471	2.5420	6.4566
4.0130	10.1930	2.4881	6.3197	3.1996	8.1269	2.5504	6.4780
4.0538	10.2966	2.4469	6.2151	3.1521	8.0063	2.5595	6.5011
4.0952	10.4018	2.3993	6.0942	3.1046	7.8856	2.5689	6.5250
4.1233	10.4731	2.3640	6.0045	3.0570	7.7647	2.5791	6.5509
4.1518	10.5455	2.3251	5.9057	3.0211	7.6735	2.5878	6.5730
4.1733	10.6001	2.2941	5.8270	2.9971	7.6126	2.5950	6.5913
4.1949	10.6550	2.2628	5.7475	2.9729	7.5511	2.6034	6.6126

Table III (cont.)

Tandem rotor mean section coordinates.

(Aft airfoil)

X		Y		X		Y	
in.	cm	in.	cm	in.	cm	in.	cm
3.1818	8.0817	2.7737	7.0451	4.3443	11.0345	2.5830	6.5608
3.1859	8.0921	2.7934	7.0952	4.3216	10.9768	2.5701	6.5280
3.1964	8.1188	2.8158	7.1521	4.3007	10.9237	2.5821	6.5585
3.2077	8.1475	2.8365	7.2047	4.2801	10.8714	2.5933	6.5869
3.2267	8.1958	2.8636	7.2735	4.2534	10.8036	2.6067	6.6210
3.2549	8.2674	2.8934	7.3492	4.2271	10.7368	2.6191	6.6825
3.2854	8.3449	2.9183	7.4124	4.1882	10.6382	2.6367	6.6972
3.3178	8.4272	2.9393	7.4658	4.1503	10.5417	2.6523	6.7368
3.3520	8.5140	2.9567	7.5100	4.1133	10.4477	2.6657	6.7708
3.3876	8.6045	2.9709	7.5460	4.0770	10.3555	2.6778	6.8016
3.4248	8.7081	2.9819	7.5740	4.0294	10.2346	2.6920	6.8376
3.4634	8.7970	2.9903	7.5953	3.9831	10.1170	2.7038	6.8676
3.5029	8.8973	2.9963	7.6106	3.9373	10.0007	2.7141	6.8938
3.5541	9.0274	3.0003	7.6207	3.8921	9.8859	2.7234	6.9174
3.6180	9.1897	2.9998	7.6194	3.8477	9.7731	2.7309	6.9364
3.6837	9.3565	2.9952	7.6078	3.7933	9.0349	2.7380	6.9545
3.7407	9.5013	2.9868	7.5864	3.7293	9.4724	2.7438	6.9692
3.7875	9.6202	2.9776	7.5631	3.6661	9.3118	2.7476	6.9789
3.8357	9.7426	2.9657	7.5328	3.6149	9.1818	2.7481	6.9801
3.8855	9.8691	2.9501	7.4932	3.5743	9.0787	2.7475	6.9786
3.9367	9.9992	2.9315	7.4450	3.5345	8.9776	2.7453	6.9730
3.9900	10.1346	2.9085	7.3875	3.4956	8.8788	2.7412	6.9626
4.0320	10.2412	2.8870	7.3829	3.4573	8.8831	2.7359	6.9491
4.0762	10.3535	2.8611	7.2671	3.4190	8.6842	2.7305	6.9354
4.1227	10.4716	2.8299	7.1879	3.3804	8.5862	2.7256	6.9230
4.1735	10.6006	2.7899	7.0863	3.3412	8.4866	2.7222	6.9143
4.2113	10.6967	2.7549	6.9974	3.3011	8.3847	2.7205	6.9100
4.2556	10.8092	2.7062	6.8737	3.2702	8.3063	2.7209	6.9110
4.2956	10.9108	2.6552	6.7442	3.2492	8.2529	2.7222	6.9143
4.3420	11.0286	2.5909	6.5808	3.2280	8.1991	2.7238	6.9184

Table III (cont.)
Tandem rotor tip section coordinates.
(Aft airfoil)

X		Y		X		Y	
in.	cm	in.	cm	in.	cm	in.	cm
3.3457	8.4980	3.1153	7.91286	4.4663	11.3444	3.0980	7.8689
3.3469	8.5011	3.1267	7.9418	4.4475	11.2966	3.0835	7.8366
3.3507	8.5107	3.1425	7.9819	4.4250	11.2395	3.0895	7.8473
3.3554	8.5227	3.1576	8.0203	4.4027	11.1828	3.0953	7.8620
3.3640	8.5445	3.1789	8.0744	4.3744	11.1109	3.1016	7.8780
3.3785	8.5813	3.2046	8.1396	4.3472	11.0418	3.1072	7.8922
3.3964	8.6268	3.2273	8.1973	4.3077	10.9415	3.1143	7.6309
3.4164	8.6776	3.2481	8.2501	4.2702	10.8463	3.1196	7.9237
3.4389	8.7348	3.2668	8.2976	4.2337	10.7535	3.1240	7.9349
3.4637	8.7292	3.2834	8.3398	4.1987	10.6648	3.1270	7.9425
3.4908	8.8666	3.2981	8.3771	4.1532	10.5491	3.1300	7.9502
3.5201	8.9410	3.3107	8.4091	4.1093	10.4376	3.1317	7.9545
3.5511	9.0197	3.3220	8.4378	4.0661	10.3278	3.1329	7.9575
3.5919	9.1234	3.3342	8.4688	4.0236	10.2199	3.1332	7.9583
3.6444	9.2567	3.3458	8.4983	3.9816	10.1132	3.1331	7.9580
3.7007	9.3997	3.3540	8.5191	3.9300	9.9822	3.1322	7.9557
3.7520	9.5300	3.3570	8.5267	3.8691	9.8275	3.1304	7.9512
3.7961	9.6420	3.3568	8.5262	3.8091	9.6751	3.1277	7.9443
3.8431	9.7614	3.3538	8.5186	3.7593	9.5486	3.1252	7.9380
3.8940	9.8907	3.3476	8.5029	3.7197	9.4480	3.1231	7.9326
3.9509	10.0352	3.3361	8.4736	3.6798	9.3466	3.1211	7.9275
4.0156	10.1996	3.3178	8.4272	3.6411	9.2483	3.1182	7.9202
4.0699	10.3375	3.2989	8.3792	3.6033	9.1523	3.1144	7.9105
4.1302	10.4907	3.2749	8.3182	3.5671	9.0604	3.1092	7.8973
4.1976	10.6619	3.2444	8.2407	3.5331	8.9740	3.1022	7.8795
4.2691	10.8435	3.2106	8.1649	3.5010	8.8925	3.0934	7.8572
4.3193	10.9701	3.1857	8.0916	3.4708	8.8158	3.0829	7.8305
4.3716	11.1038	3.1589	8.0236	3.4487	8.7596	3.0746	7.8094
4.4132	11.2095	3.1368	7.9674	3.4341	8.7226	3.0691	7.7955
4.4599	11.3281	3.1103	7.9001	3.4193	8.6850	3.0636	7.7815

Table IV.
Design operating point blade loads.

$N/\sqrt{\theta}_{cr}$ = 4660 rpm (487.99 rad/sec)

P_{To}/P_{T3} = 2.01

	Forward airfoil				Aft airfoil			
	Lift		Drag*		Lift		Drag*	
	lb/in.	N/cm	lb/in.	N/cm	lb/in.	N/cm	lb/in.	N/cm
Hub	6.20	10.84	-4.07	-7.12	4.95	8.66	2.14	3.74
Mean	7.05	12.33	-2.22	-3.88	6.99	12.23	4.91	8.59
Tip	5.87	10.26	1.28	2.24	6.74	11.79	5.78	10.11

*Positive drag is in the downstream direction.

Table V.
Blade stress and deflection analysis results.

$N/\sqrt{\theta}_{cr}$ = 4660 rpm (487.99 rad/sec)

P_{To}/P_{T3} = 2.01

Forward airfoil max stress = 32,800 lb/in.^{2} (57,367 N/cm^2)

Aft airfoil max stress = 19,800 lb/in.^{2} (34,630 N/cm^2)

	Forward airfoil blade deflection				Aft airfoil blade deflection			
	δ_x		δ_u		δ_x		δ_u	
	in.	cm	in.	cm	in.	cm	in.	cm
Hub	0	0	0	0	0	0	0	0
Mean	-0.0024	-.0001	-0.0022	-.0056	-0.0022	-.0056	-0.0020	-.0051
Tip	-0.0069	-.0175	-0.0062	-.0157	-0.0066	-.0168	-0.0063	-.0160

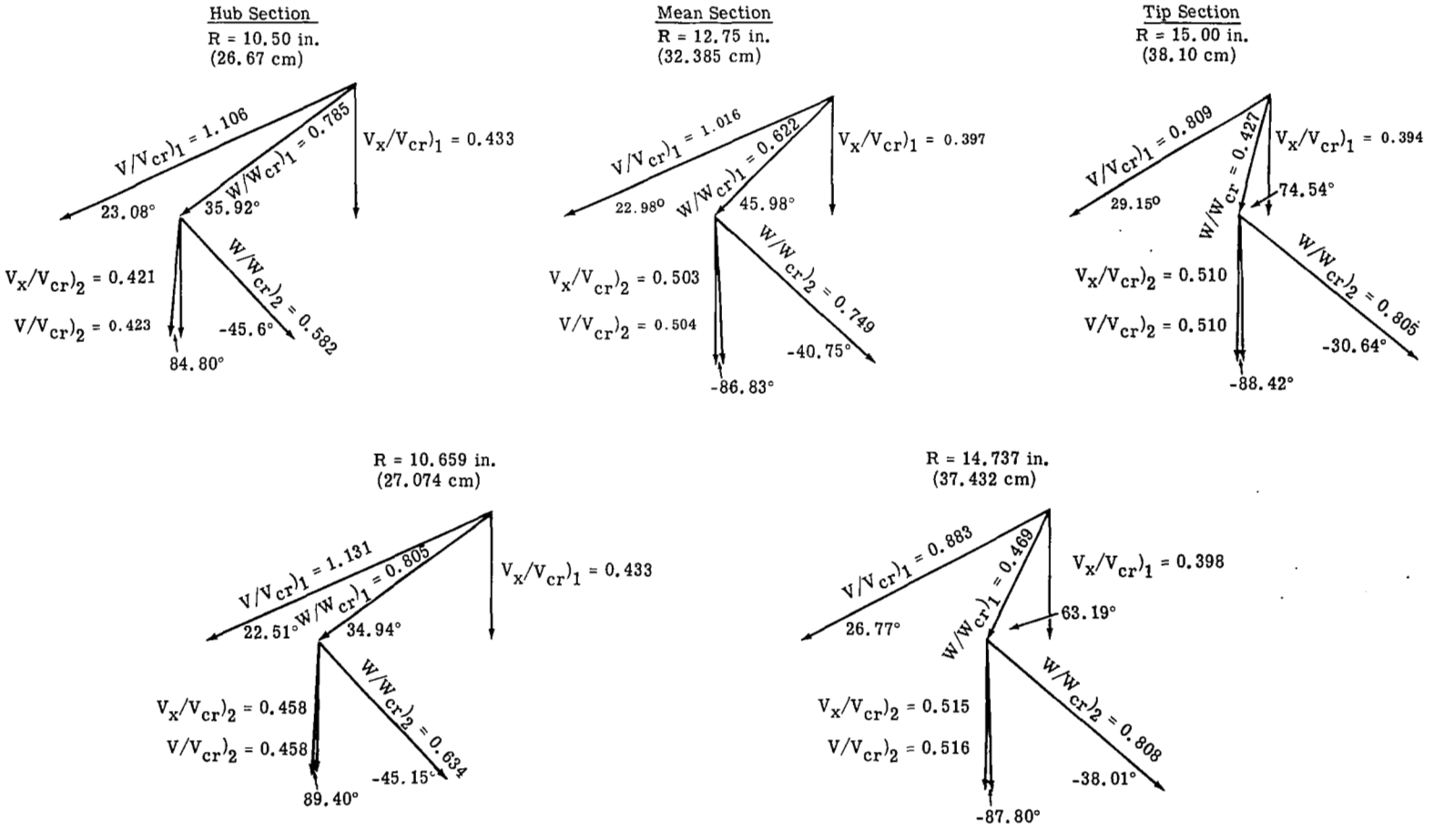

Figure 1. Design velocity diagrams of low solidity tandem rotor blade.

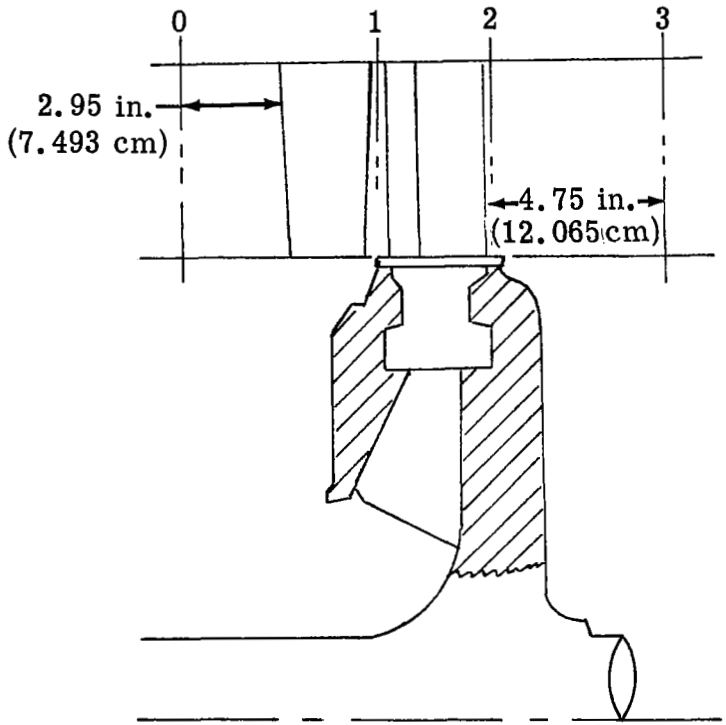

a. Schematic of flowpath

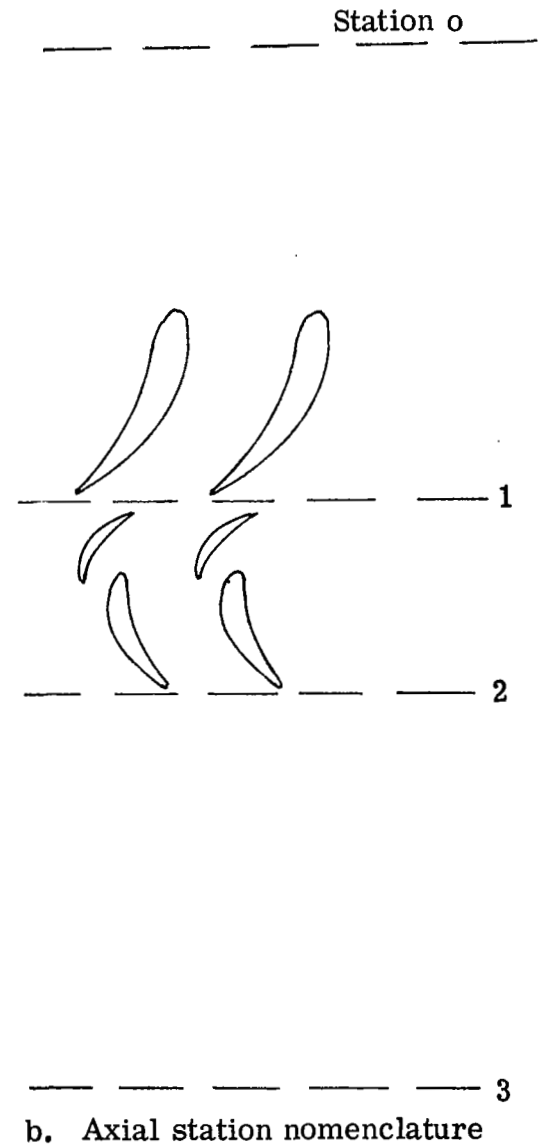

b. Axial station nomenclature

Figure 2. Tandem turbine station nomenclature.

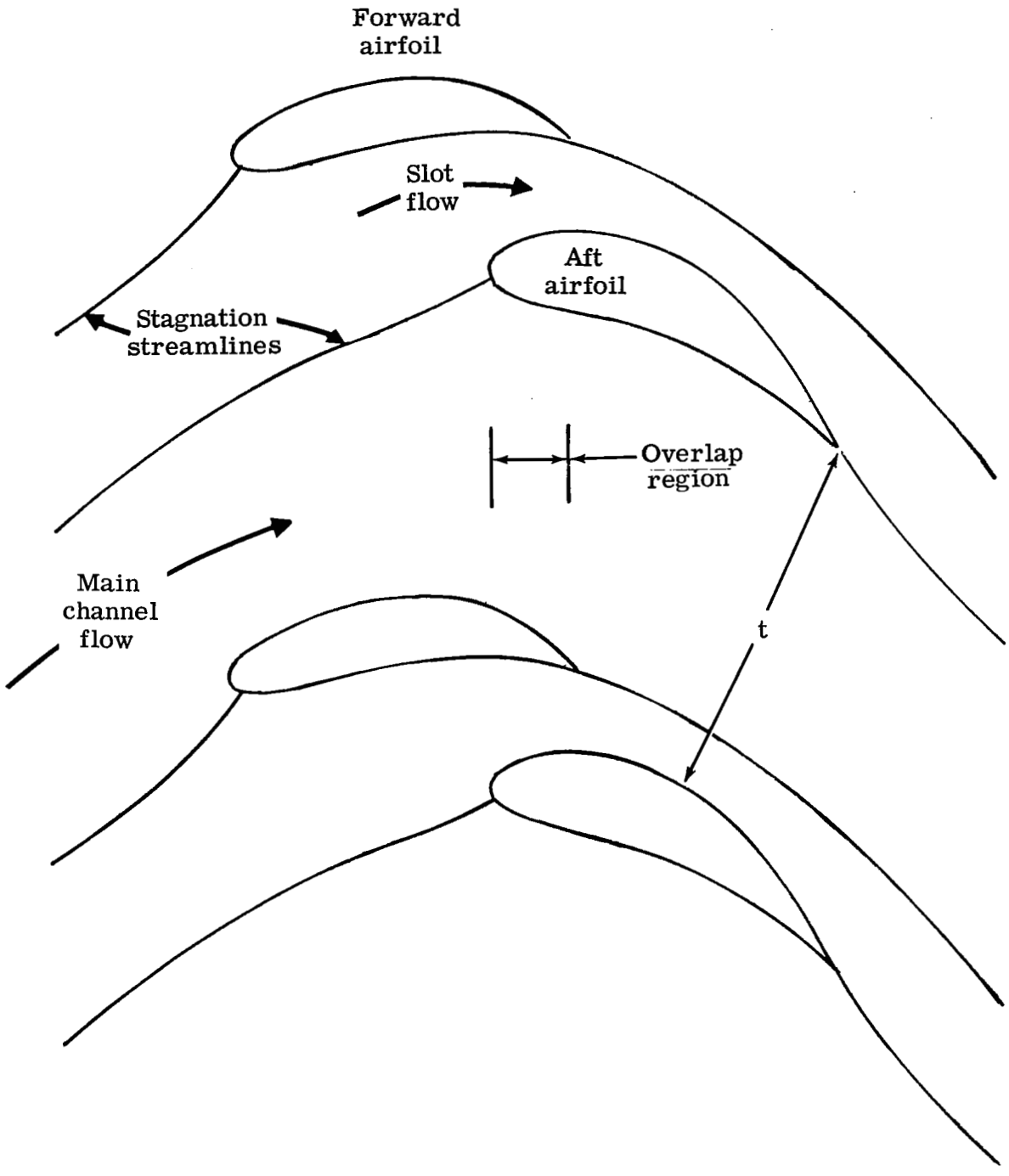

Figure 3. Schematic of tandem blade configuration.

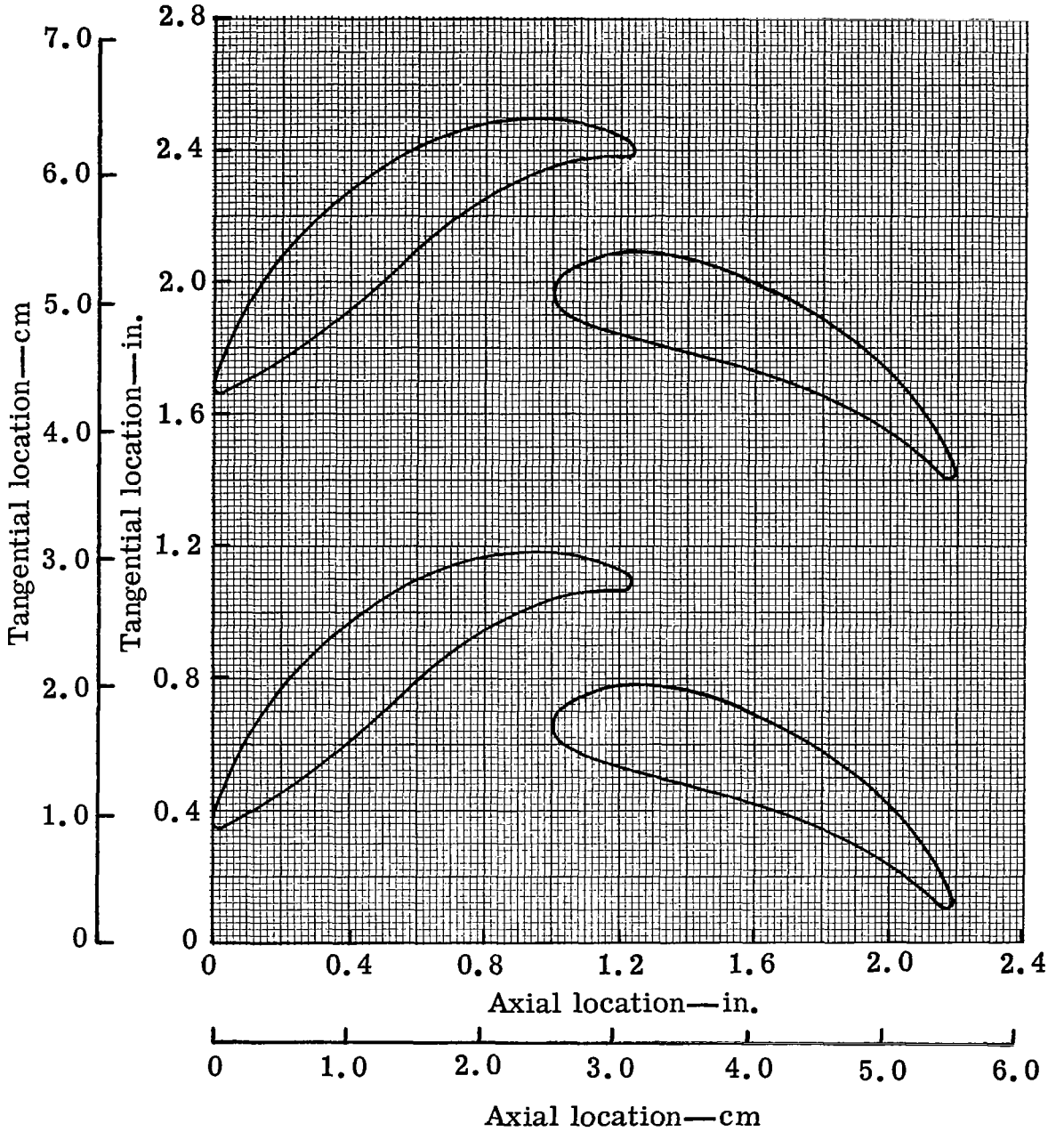

Figure 4. Tandem blade hub section profile and passage geometry.

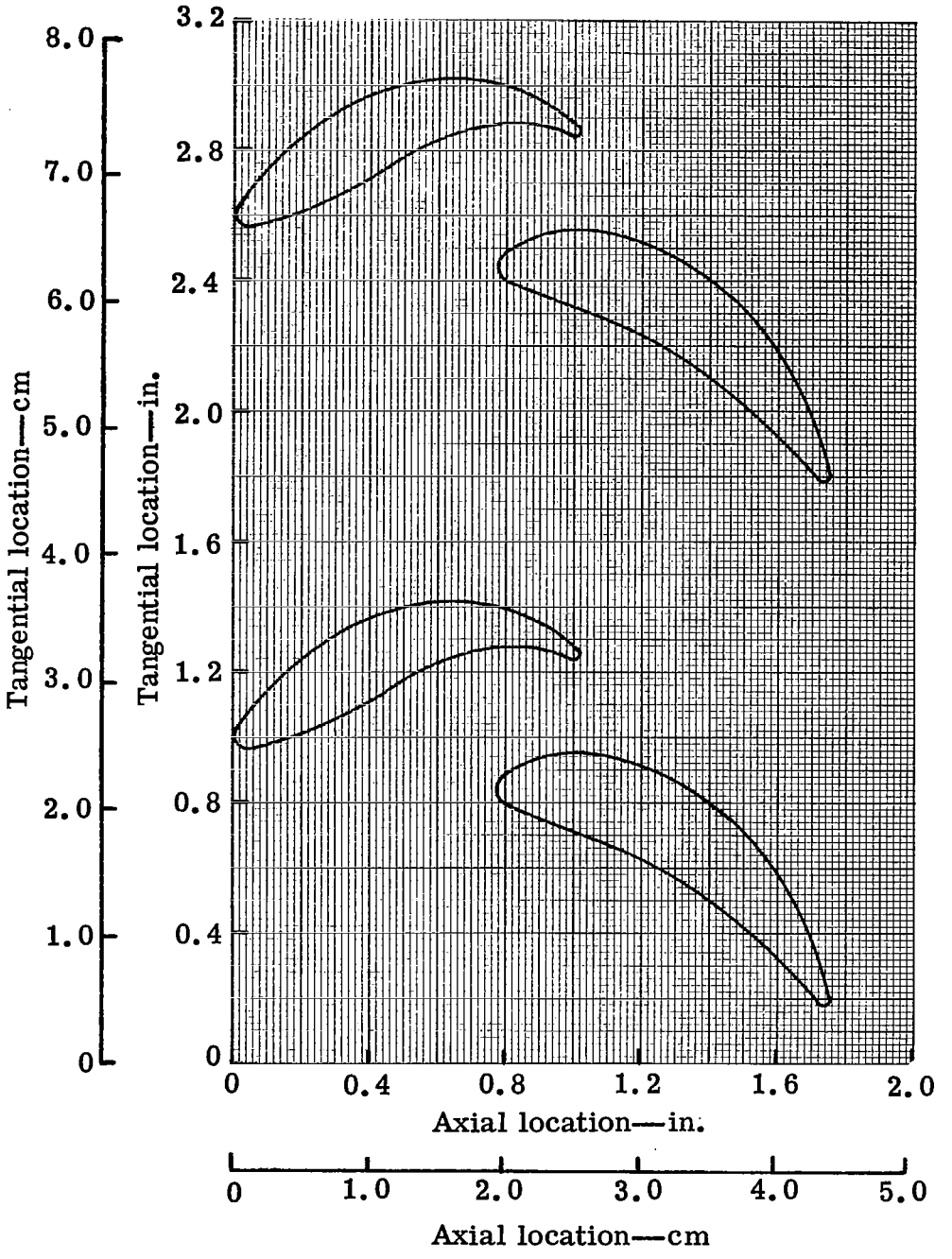

Figure 5. Tandem blade mean section profile and passage geometry.

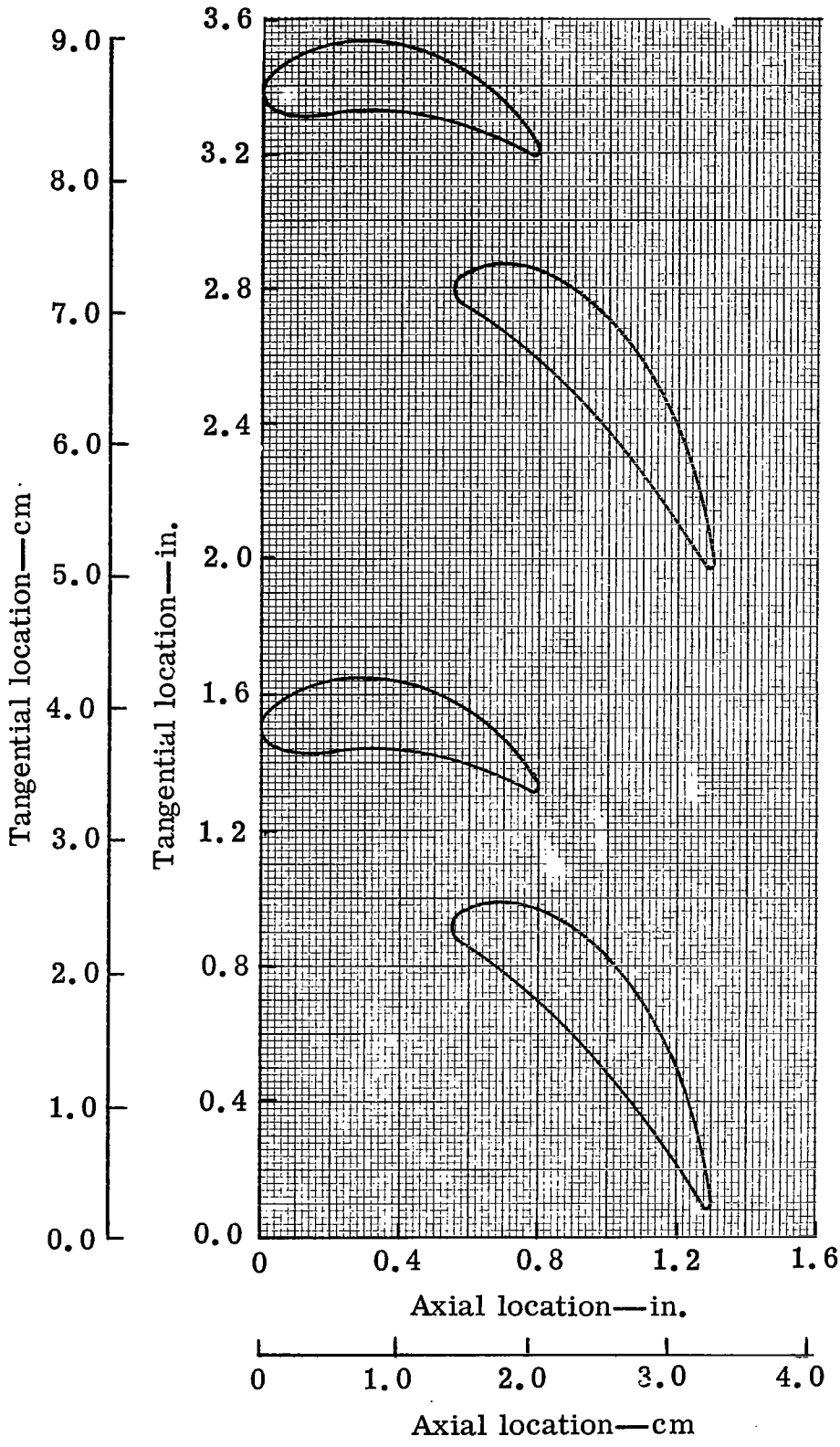

Figure 6. Tandem blade tip section profile and passage geometry.

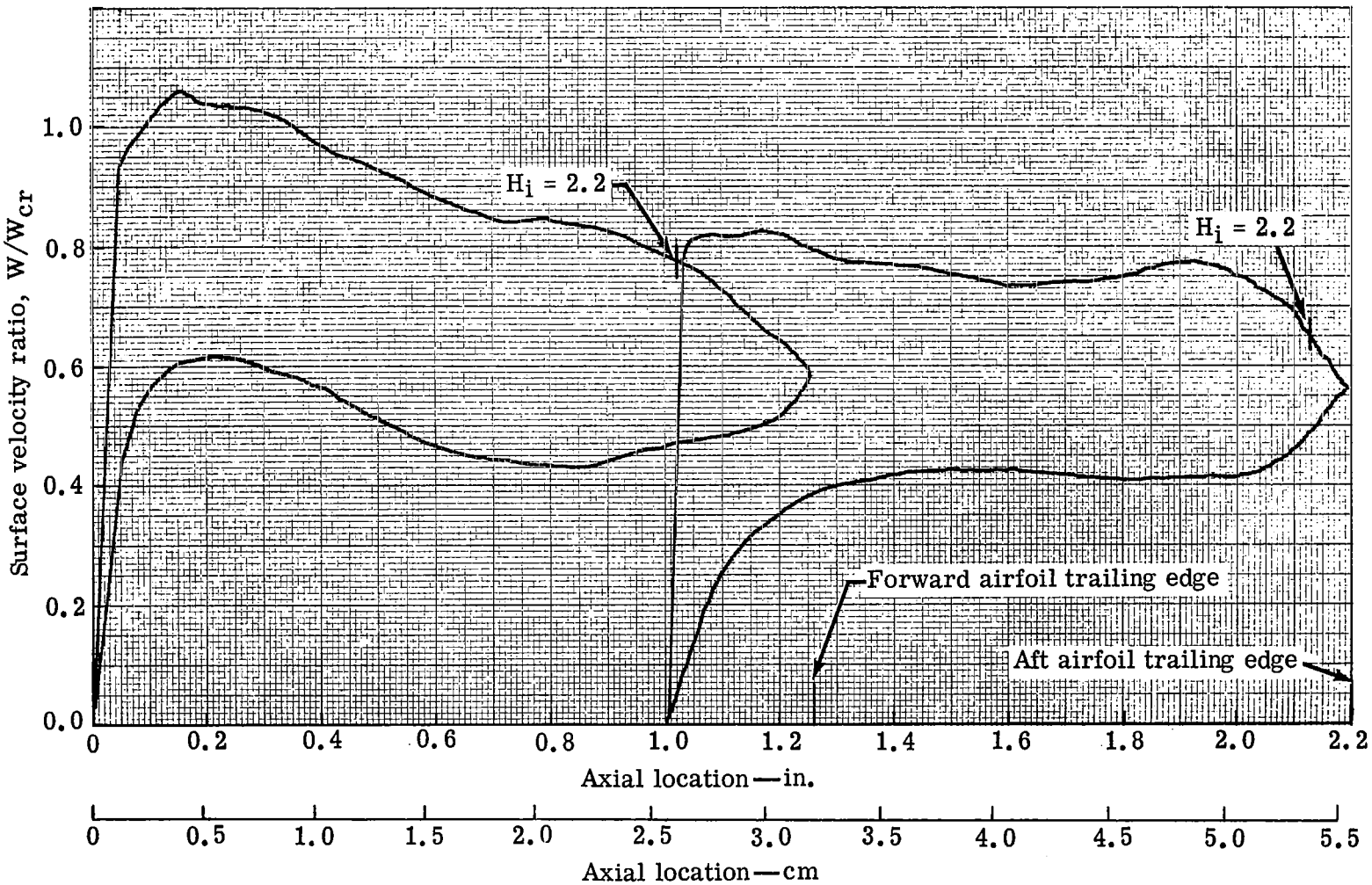

Figure 7. Tandem blade hub section predicted surface critical velocity ratio distribution.

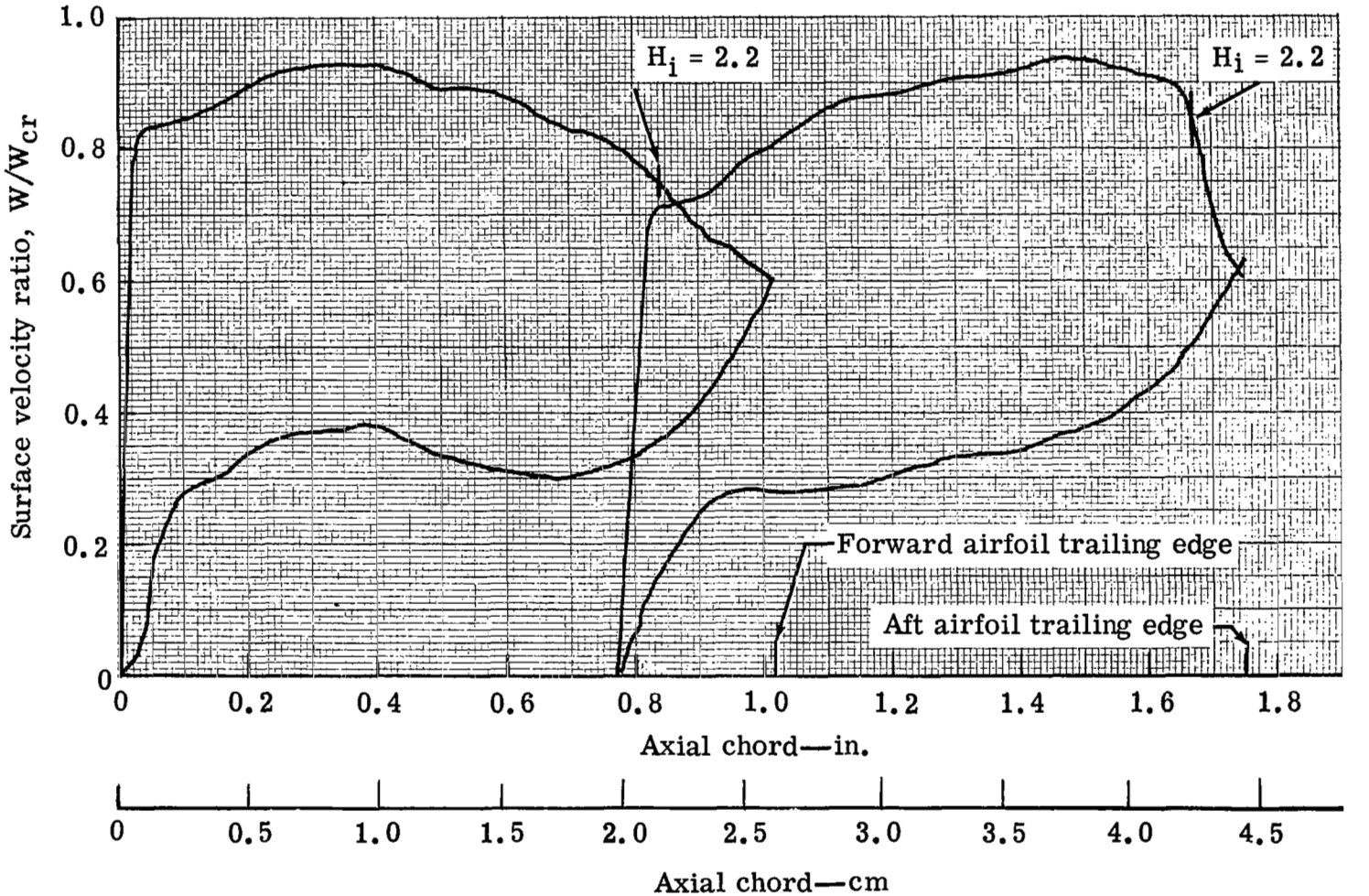

Figure 8. Tandem blade mean section predicted surface critical velocity ratio distribution.

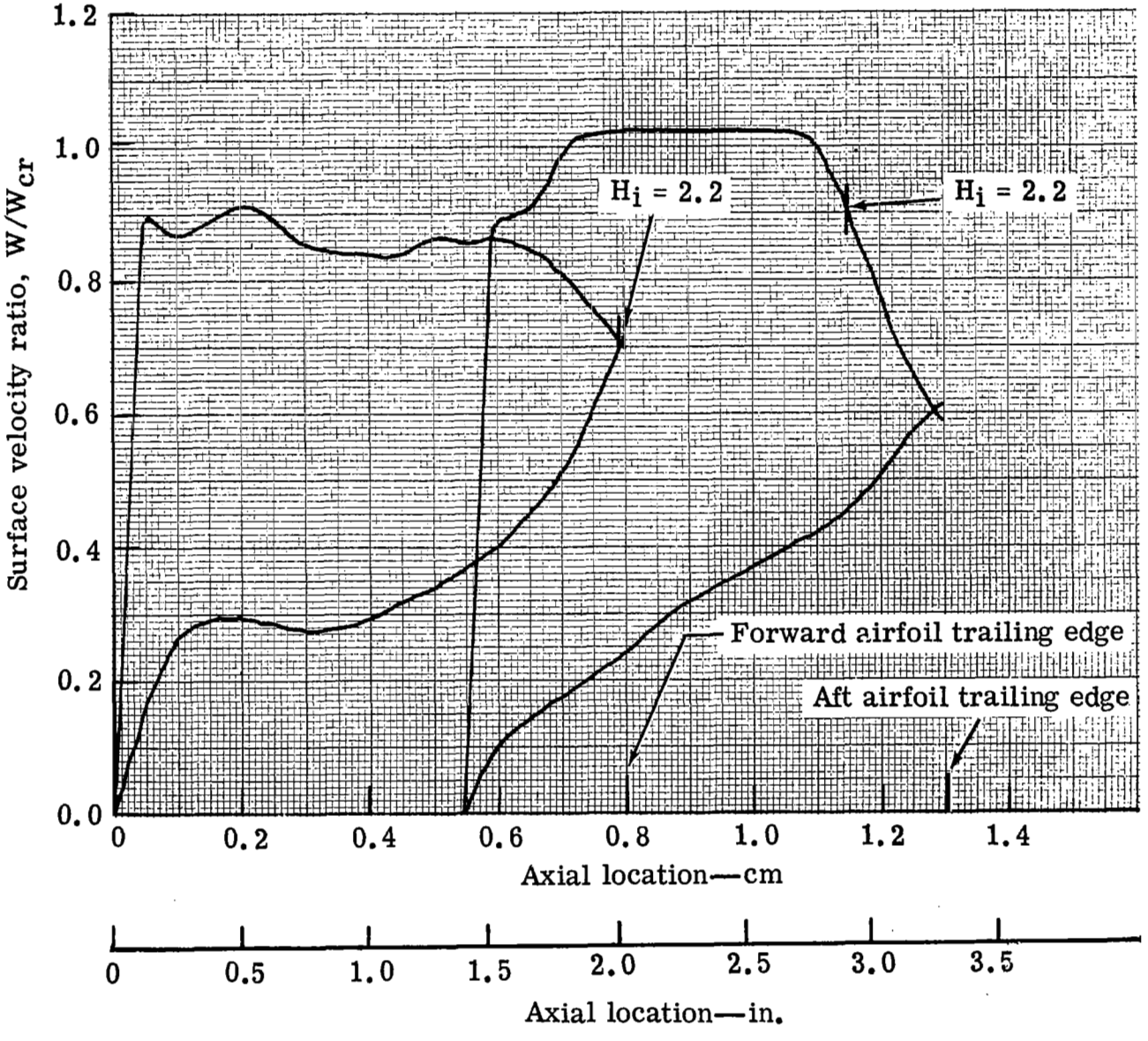

Figure 9. Tandem blade tip section predicted surface critical velocity ratio distribution.

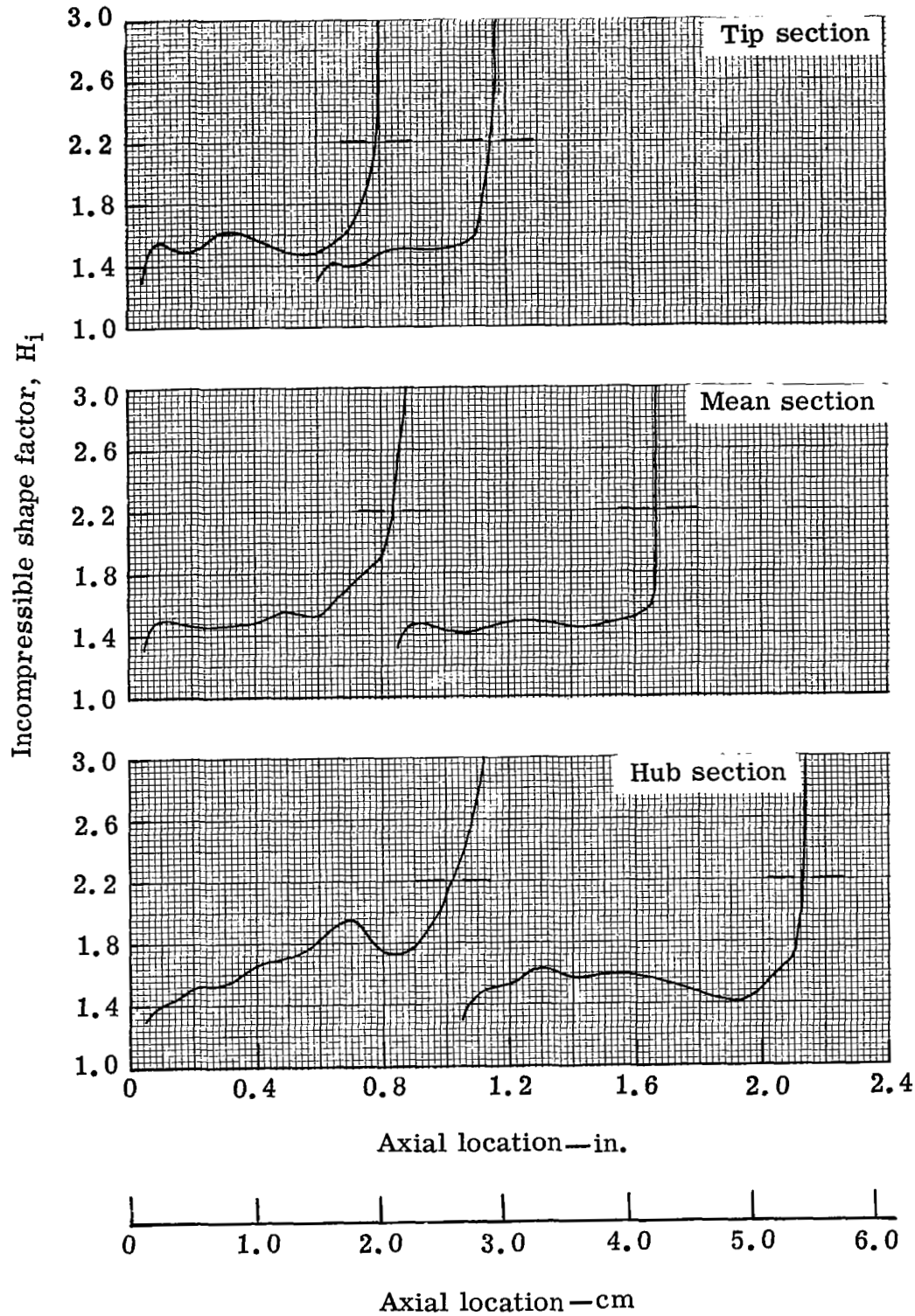

Figure 10. Predicted incompressible shape factor of the low solidity tandem blade.

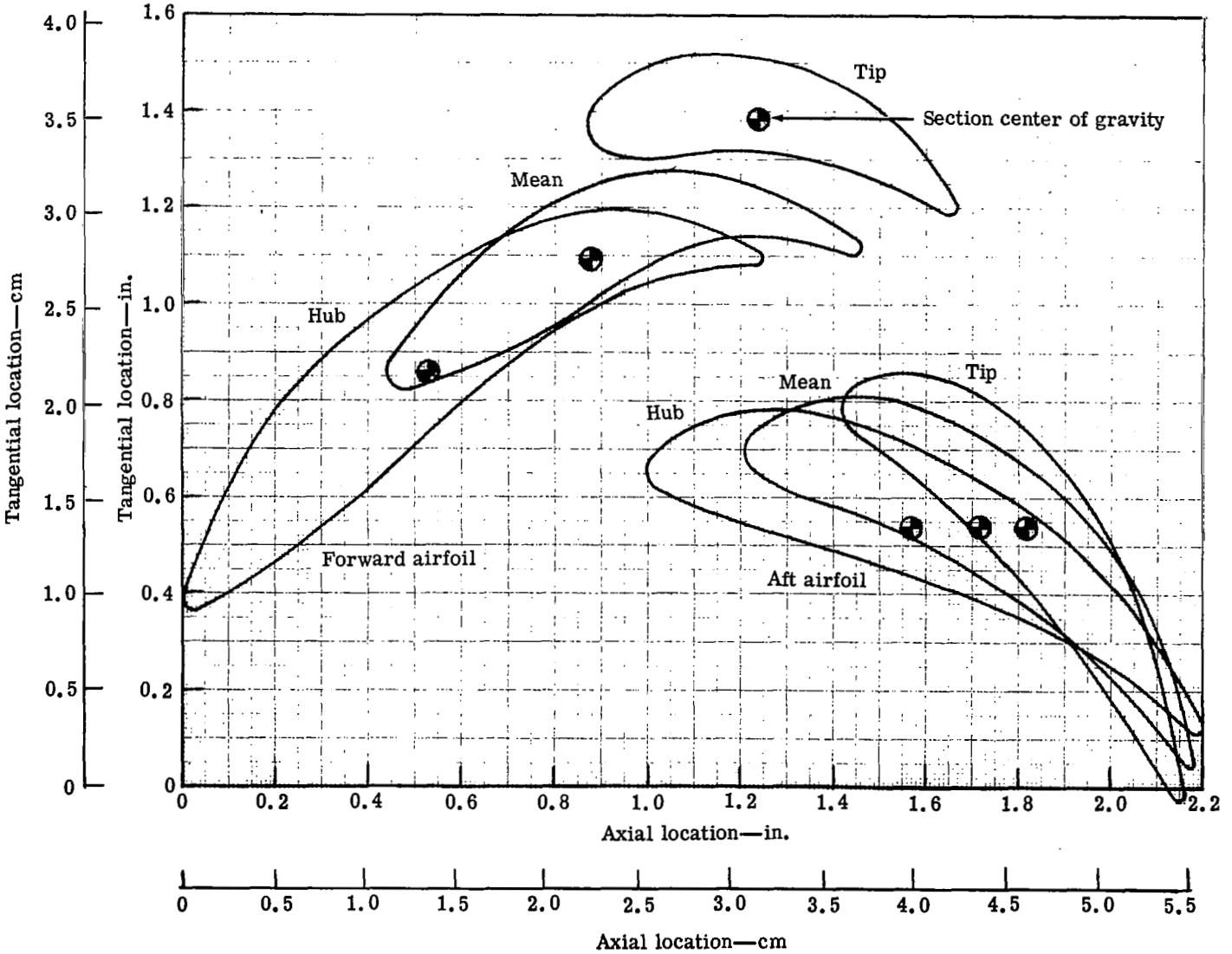

Figure 11. Radial stack arrangement of low solidity tandem blade.

Figure 12. Low solidity tandem blade rotor assembly.

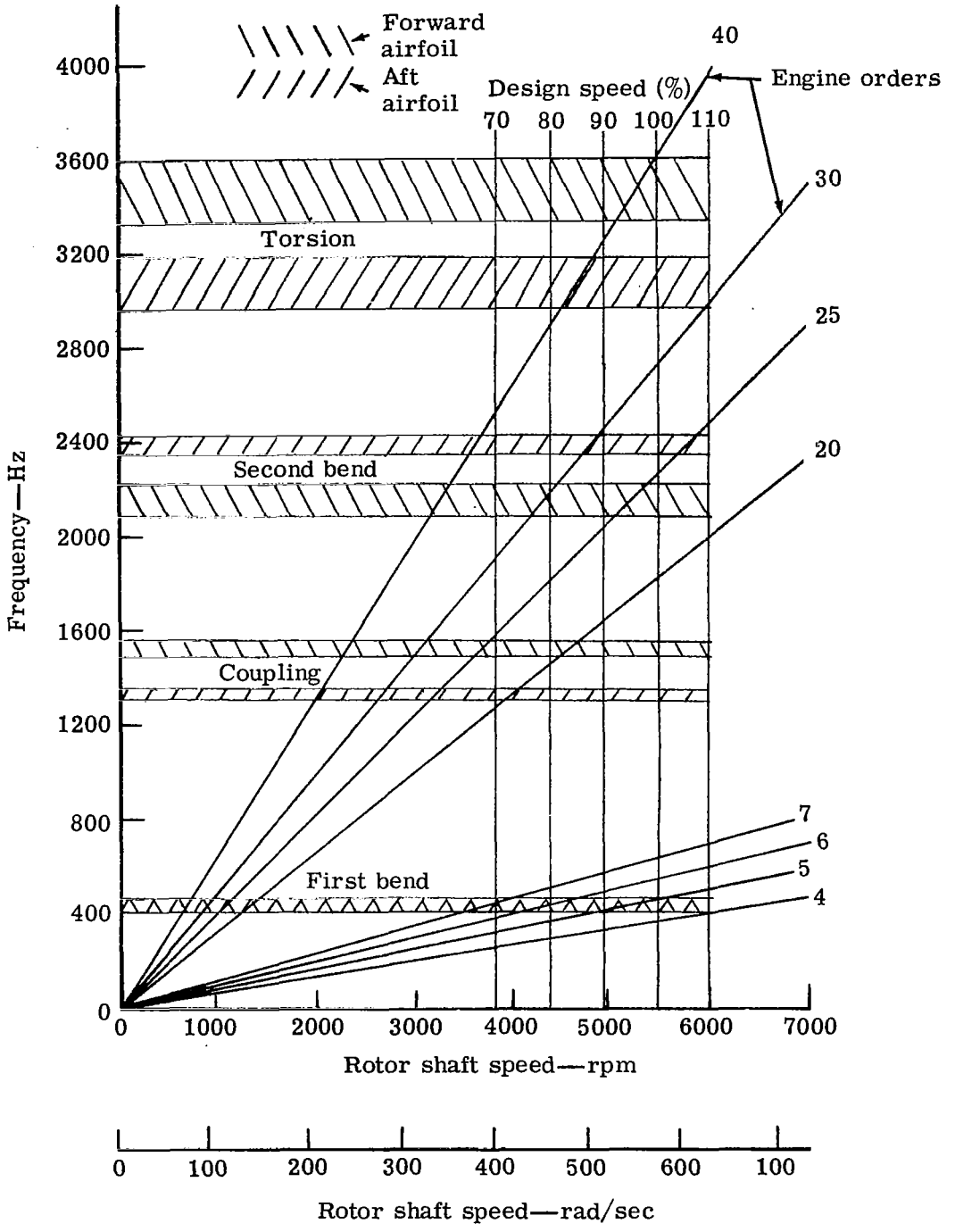

Figure 13. Low solidity tandem forward and aft airfoil vibrational characteristics.

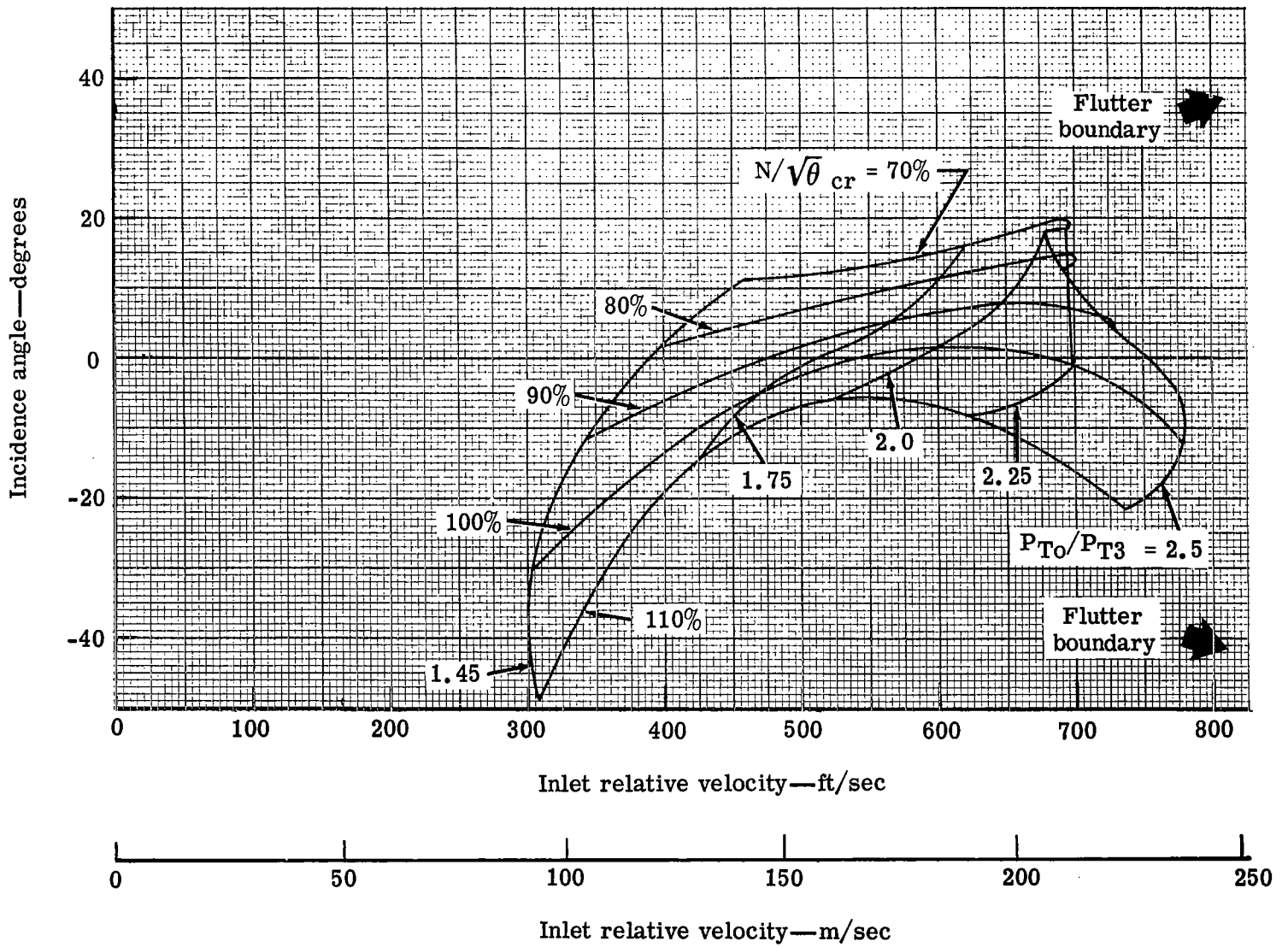

Figure 14. Low solidity tandem blade forward airfoil flutter analysis.

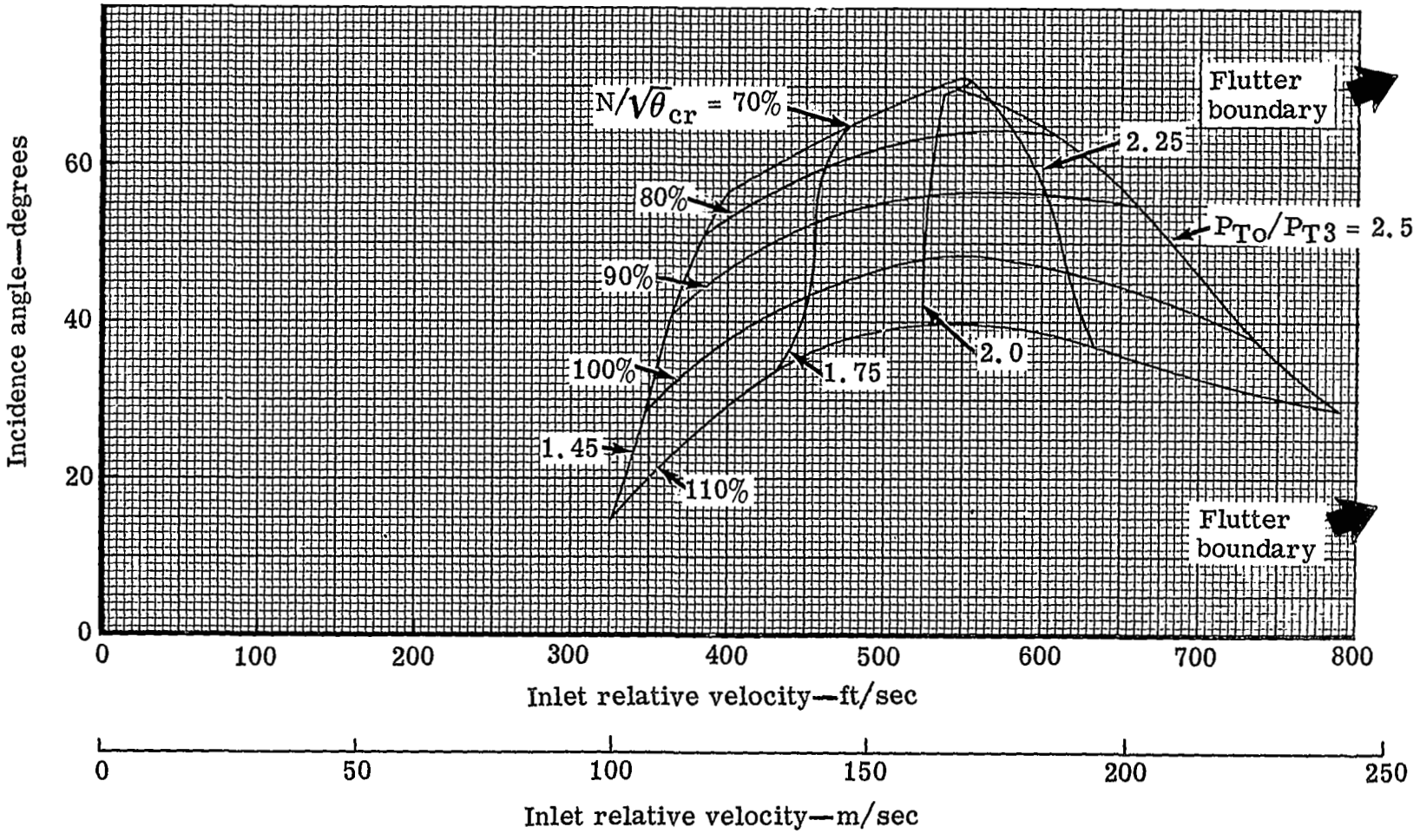

Figure 15. Low solidity tandem blade aft airfoil flutter analysis.

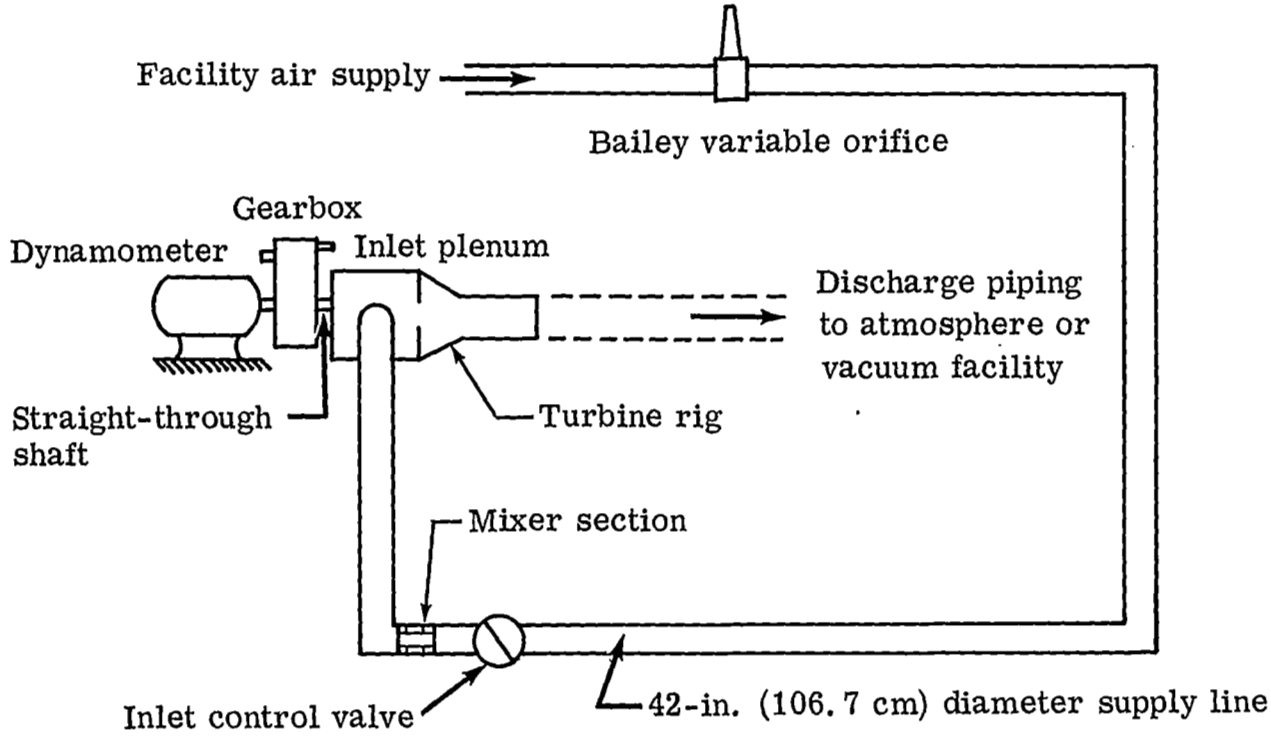

Figure 16. Schematic of test rig and air supply system.

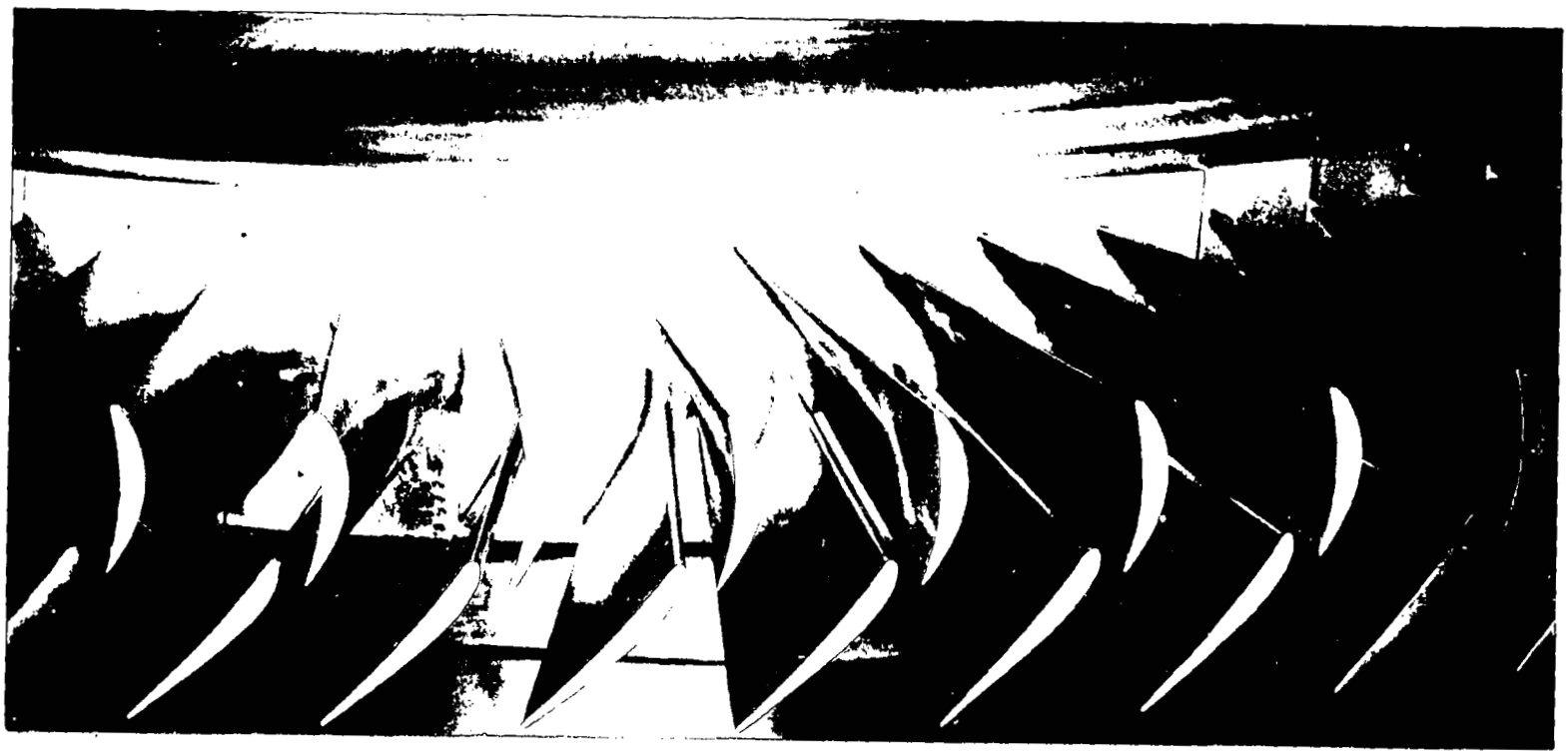

Figure 17. High solidity modified tandem blade rotor.

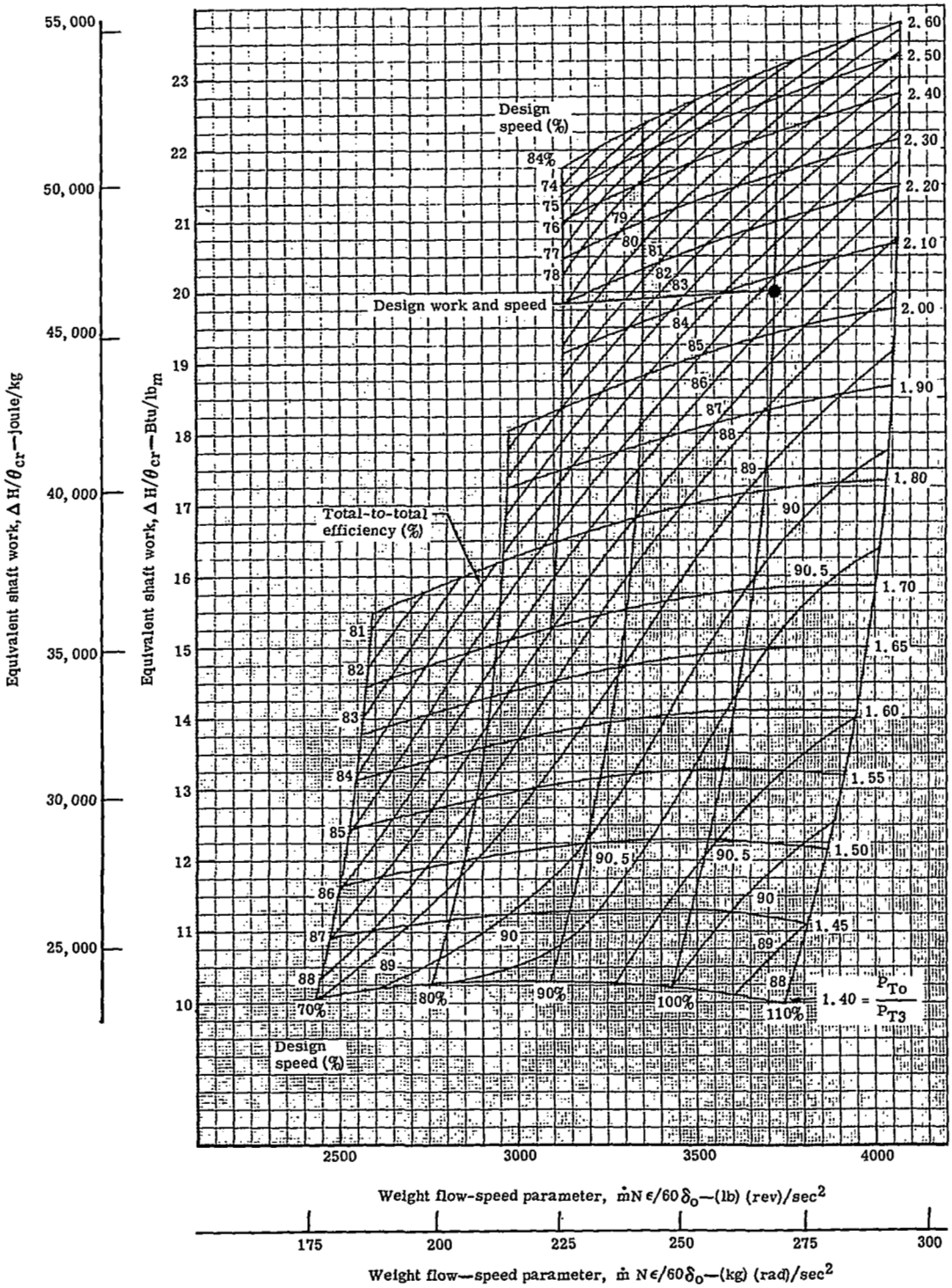

Figure 18. Overall performance of low solidity tandem rotor blade turbine.

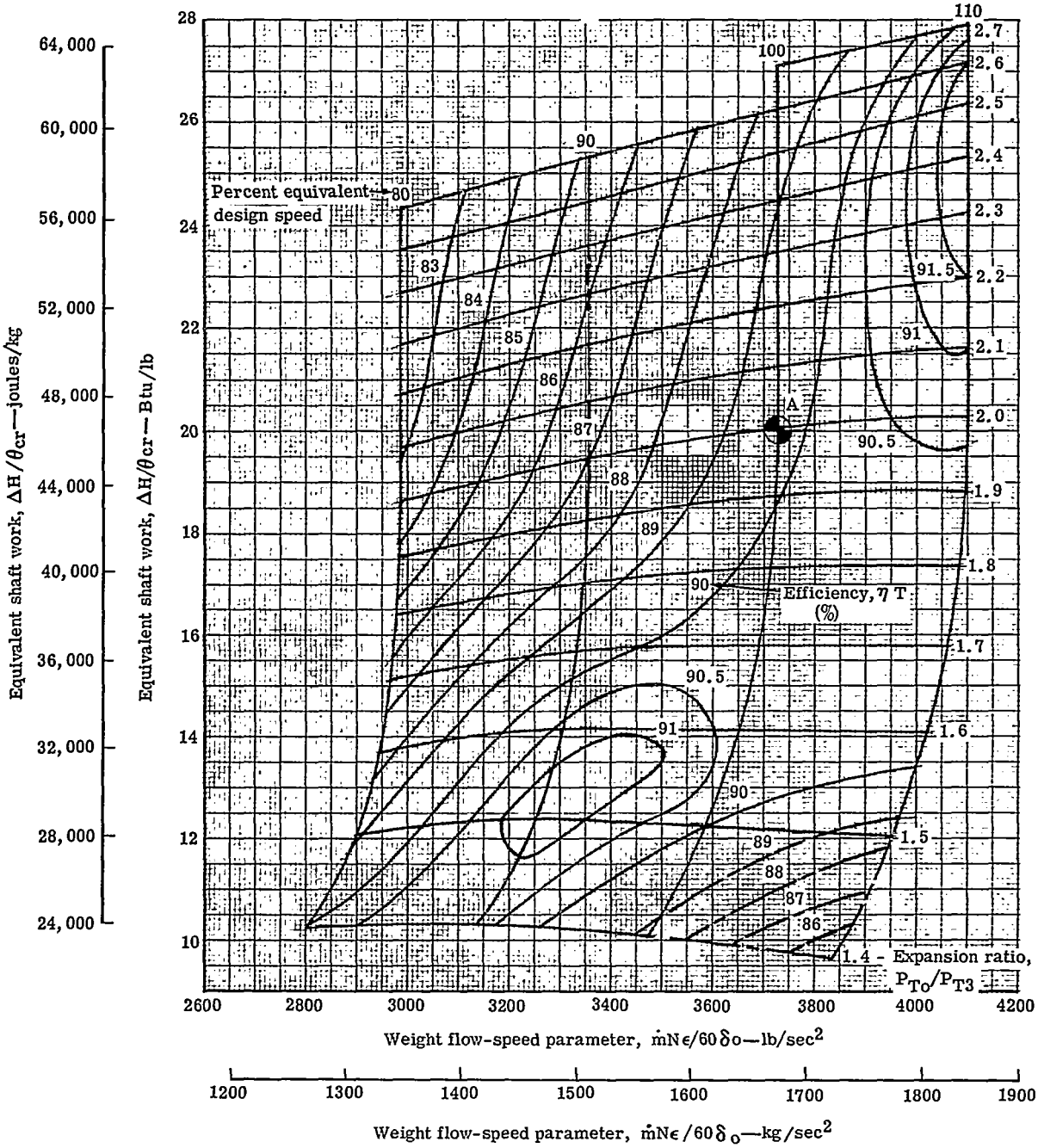

Figure 19. Overall performance of modified tandem rotor blade turbine.

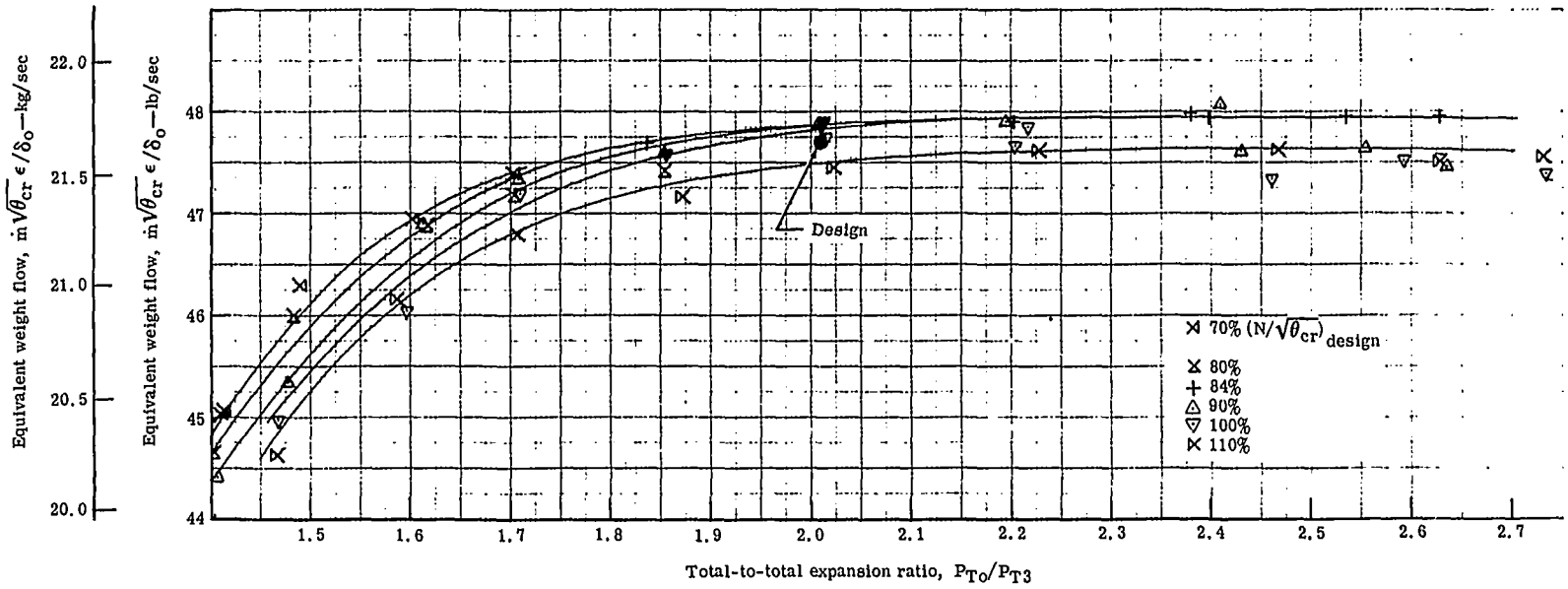

Figure 20. Variation of equivalent flow with expansion ratio and equivalent speed for low solidity tandem blade.

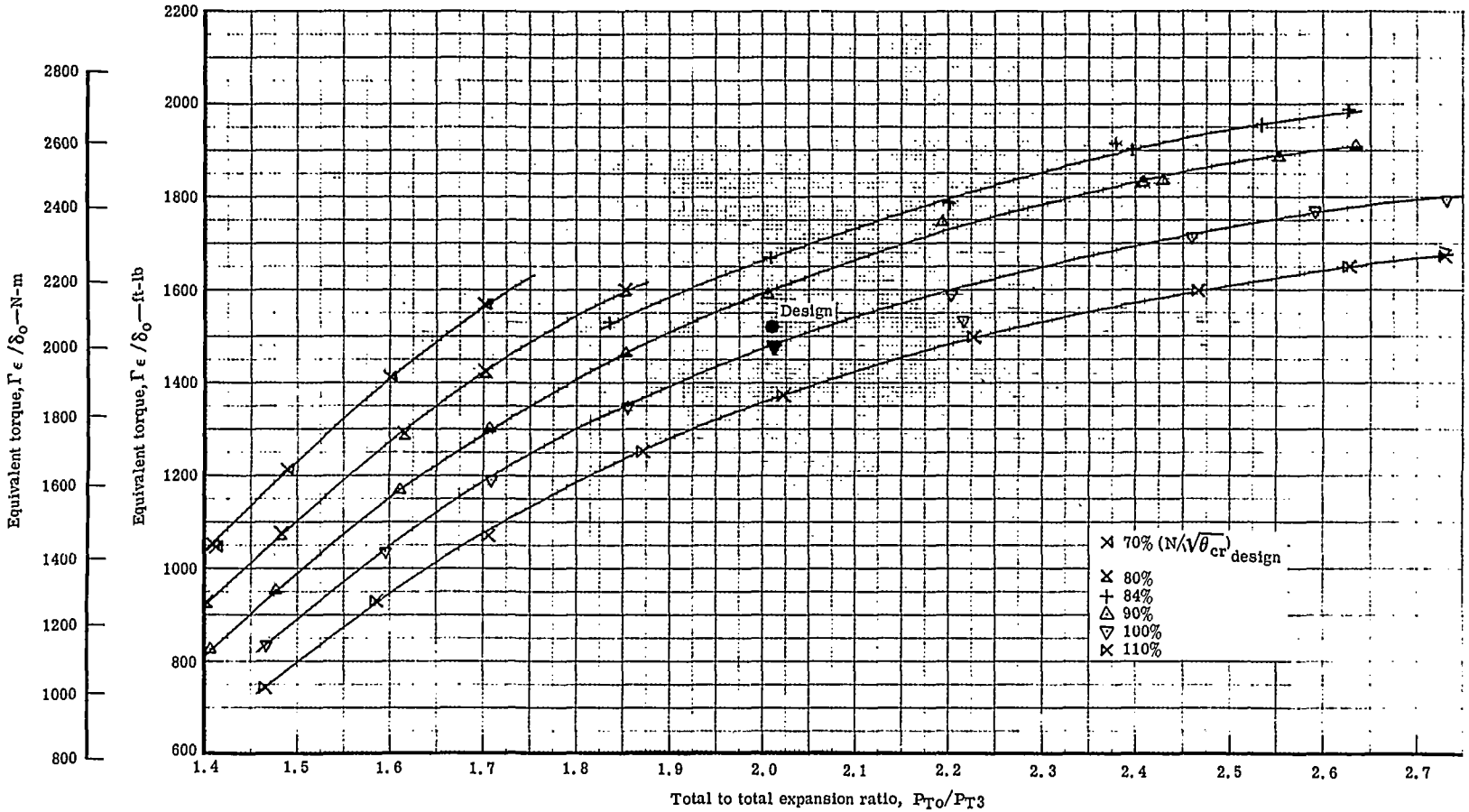

Figure 21. Variation of equivalent torque with expansion ratio and rotor speed for low solidity tandem blade.

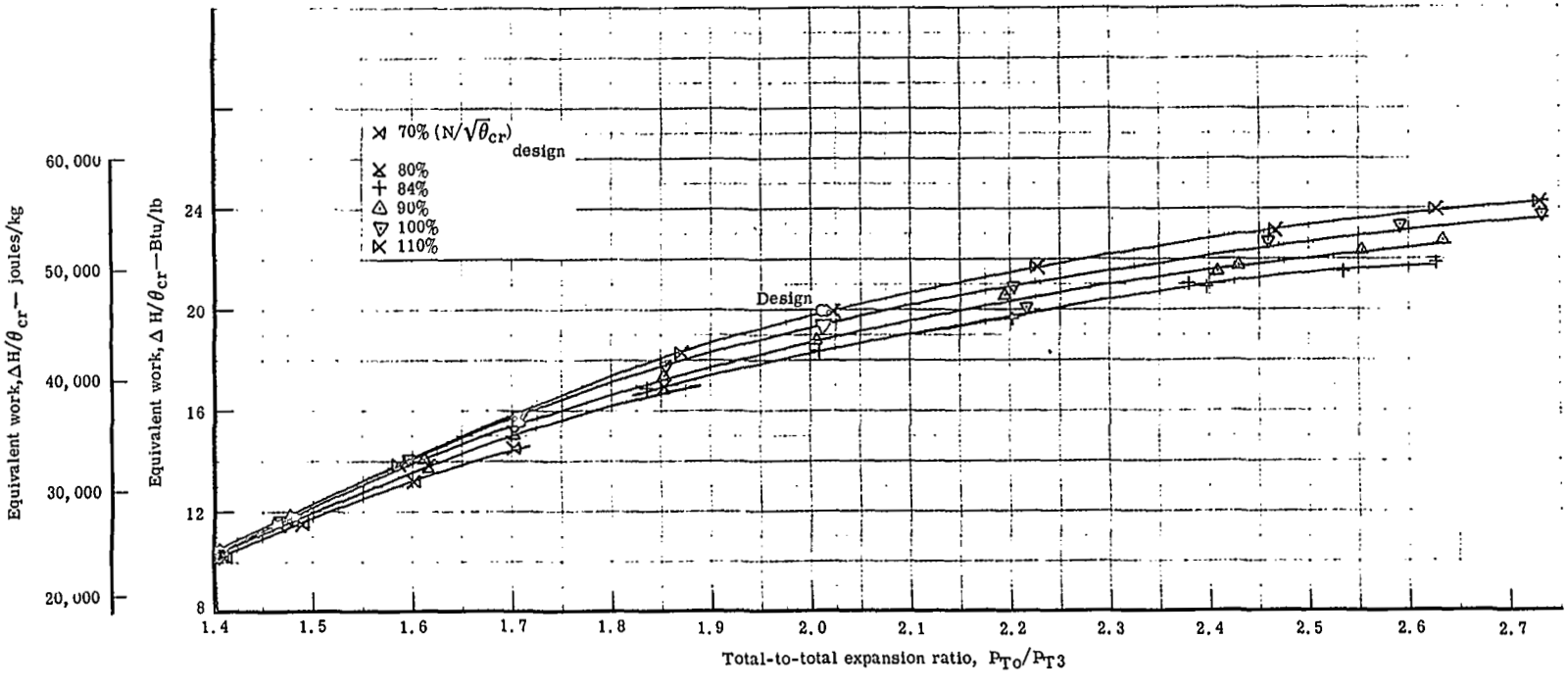

Figure 22. Variation of equivalent work with expansion ratio for lines of constant equivalent speed for low solidity tandem blade.

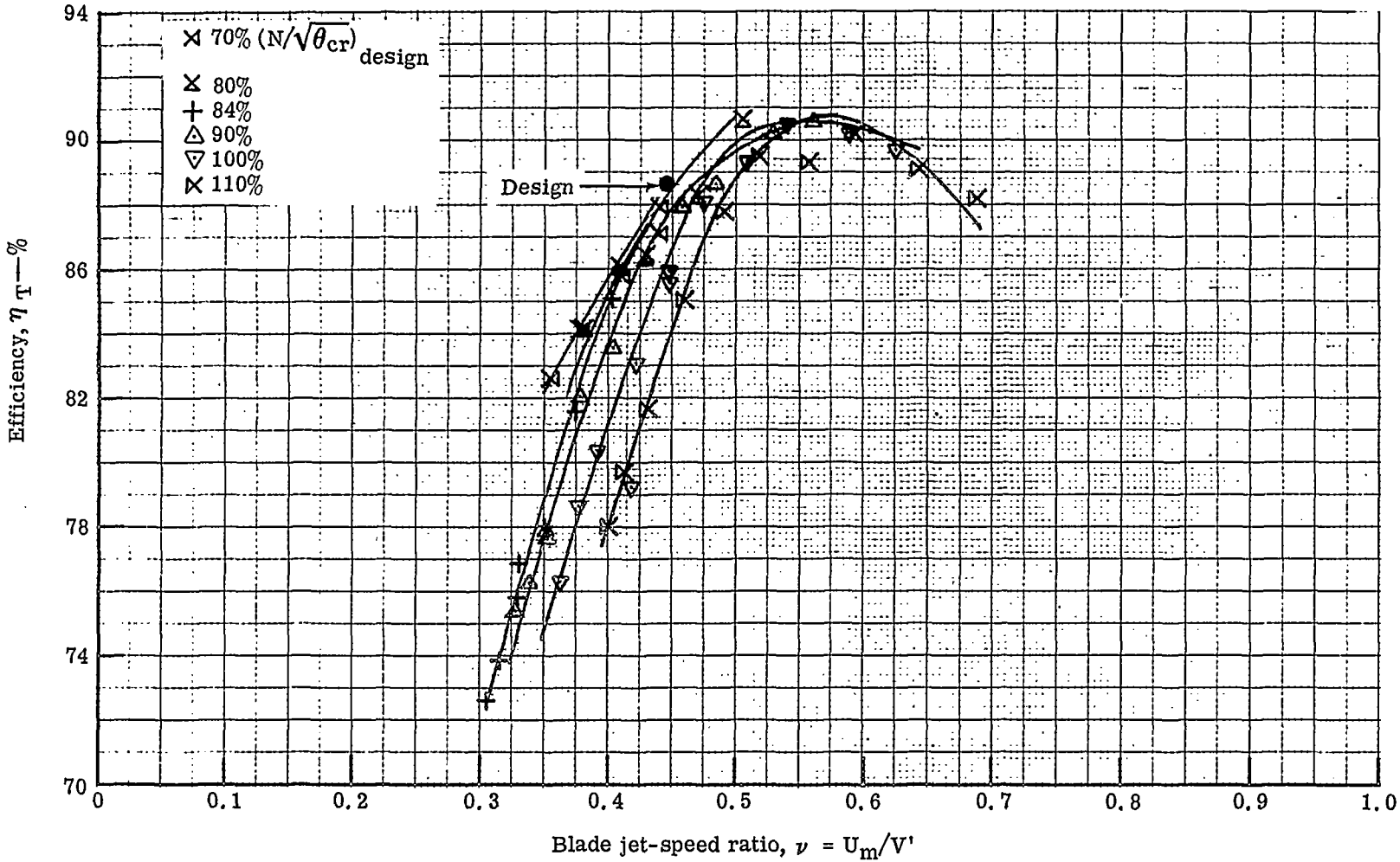

Figure 23. Variation of efficiency with blade-jet speed ratio for lines of constant equivalent speed for low solidity tandem blade.

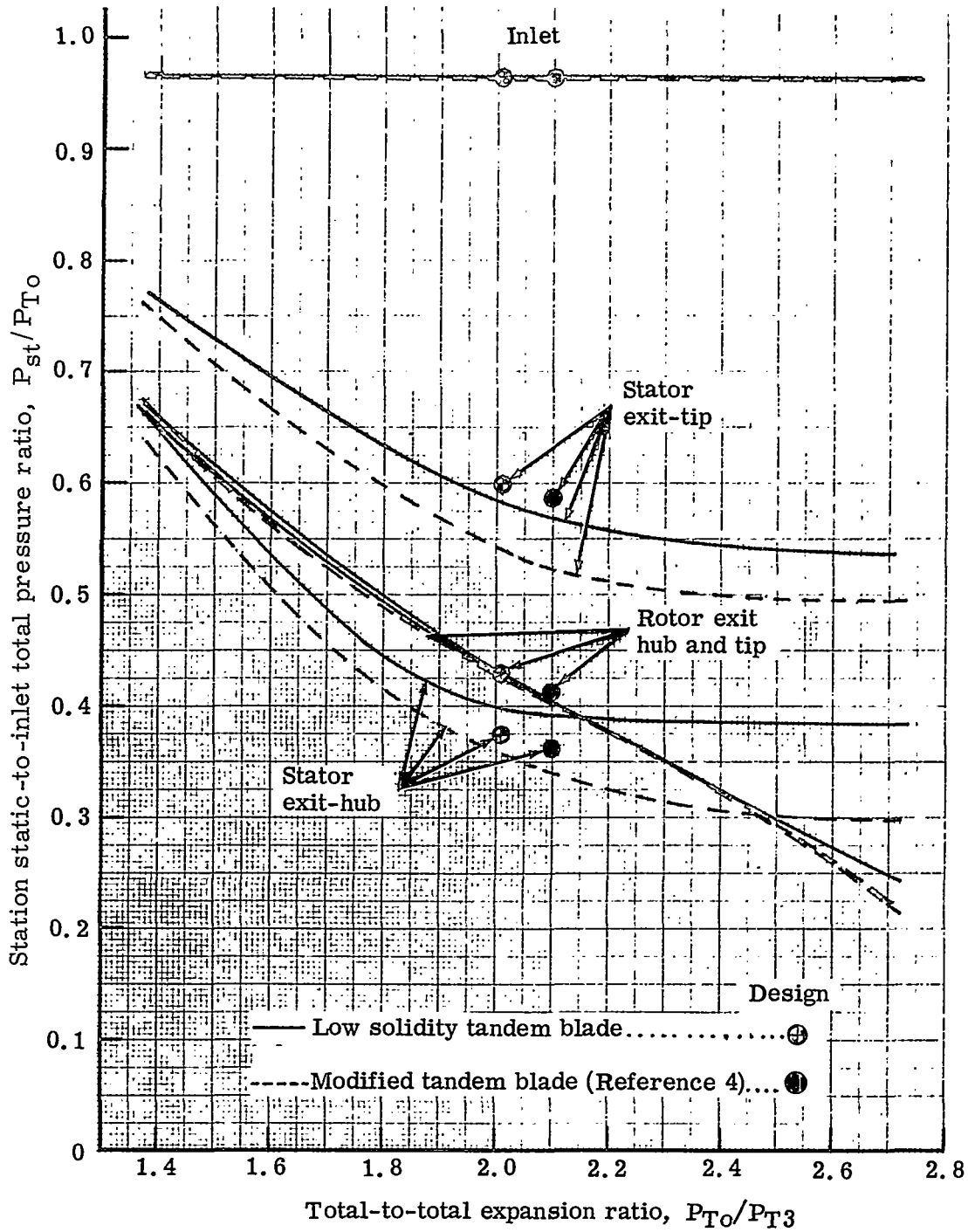

Figure 24. Comparison of low solidity and modified tandem turbine static pressure with turbine expansion ratio at design equivalent speed.

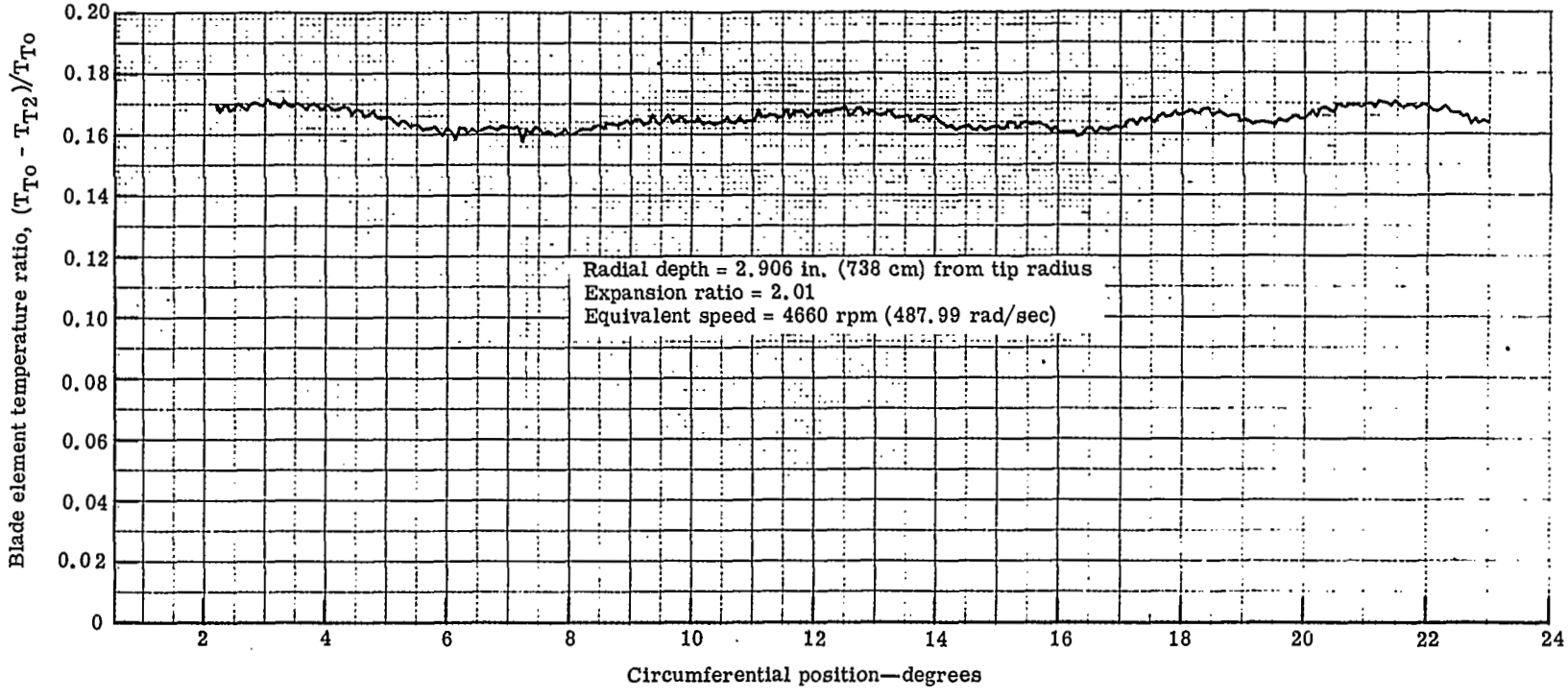

Figure 25. Circumferential variation of blade element temperature ratio at rotor exit.

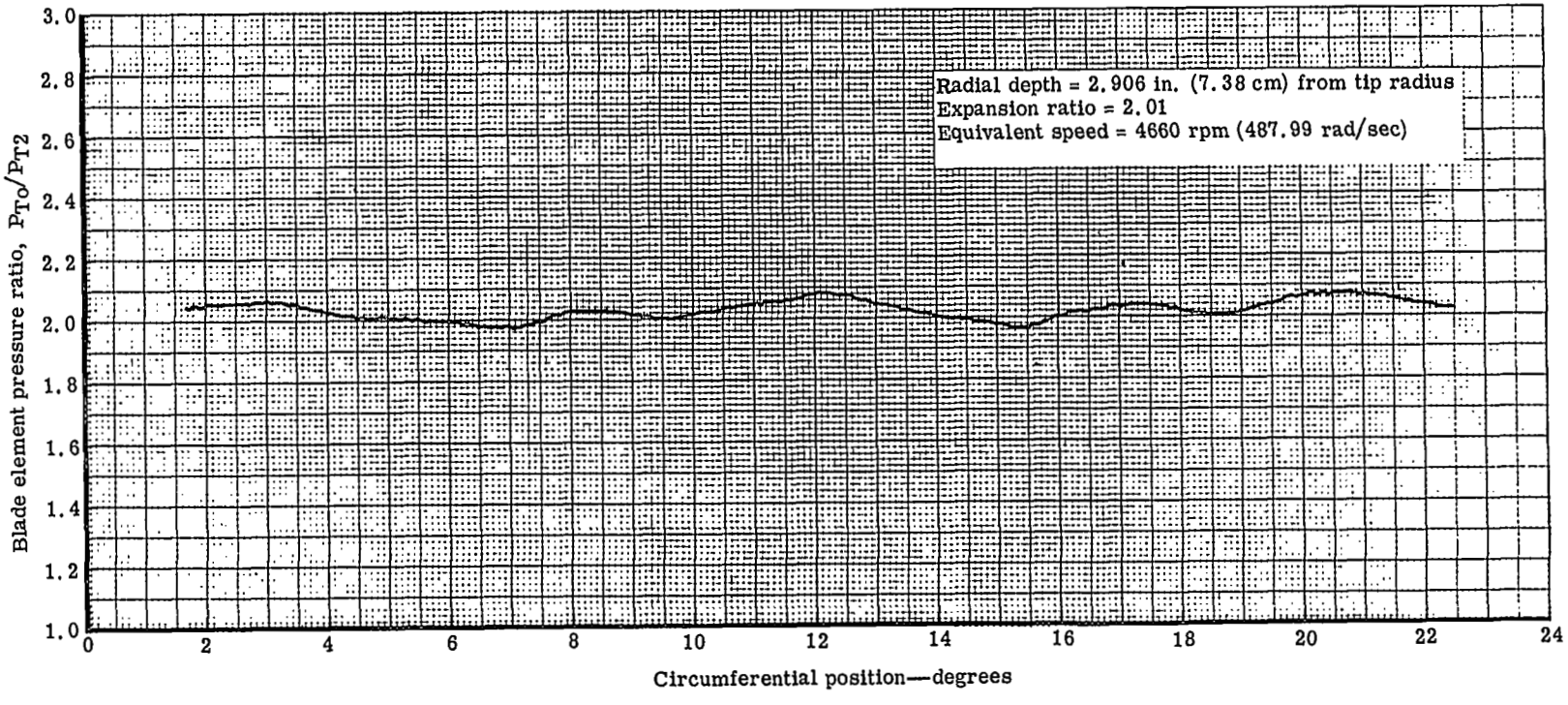

Figure 26. Circumferential variation of blade element total pressure ratio at rotor exit.

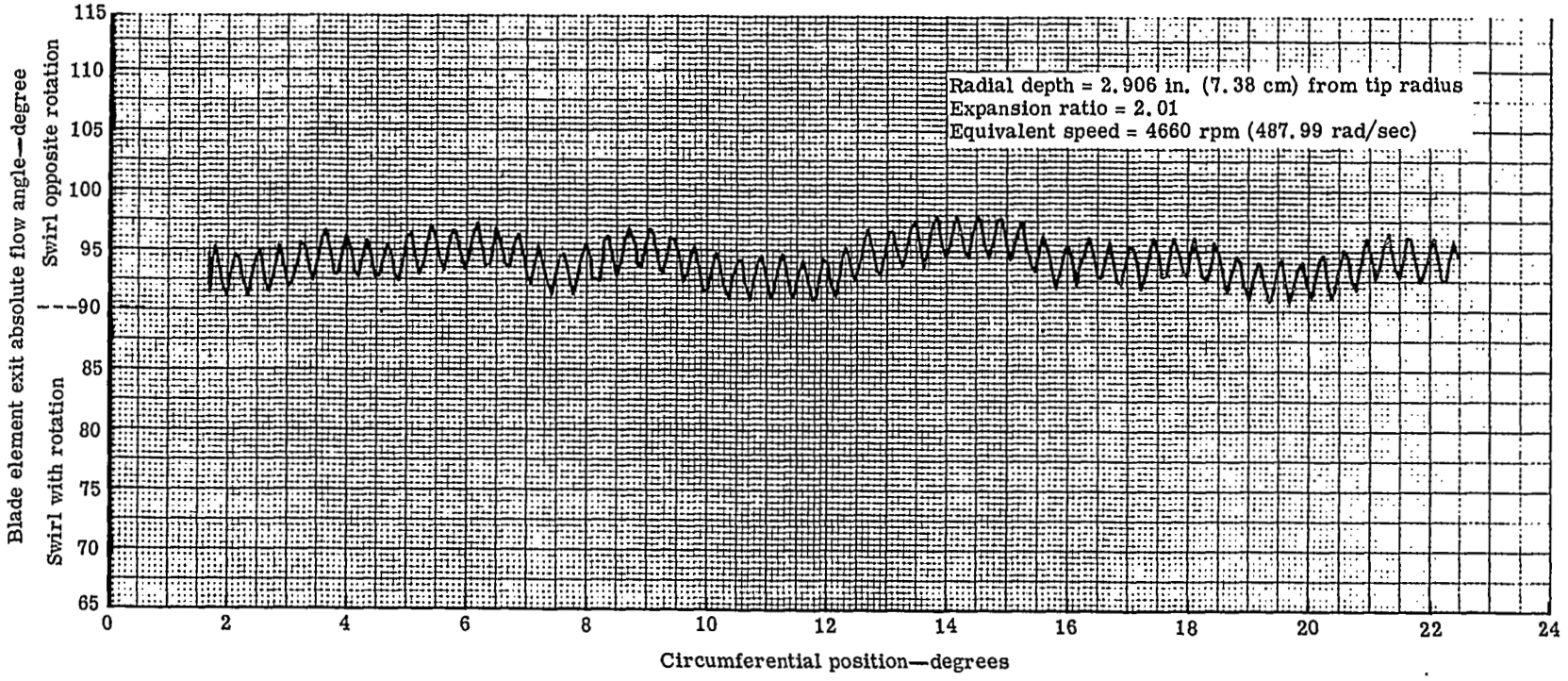

Figure 27. Circumferential variation of blade element exit absolute flow angle at rotor exit.

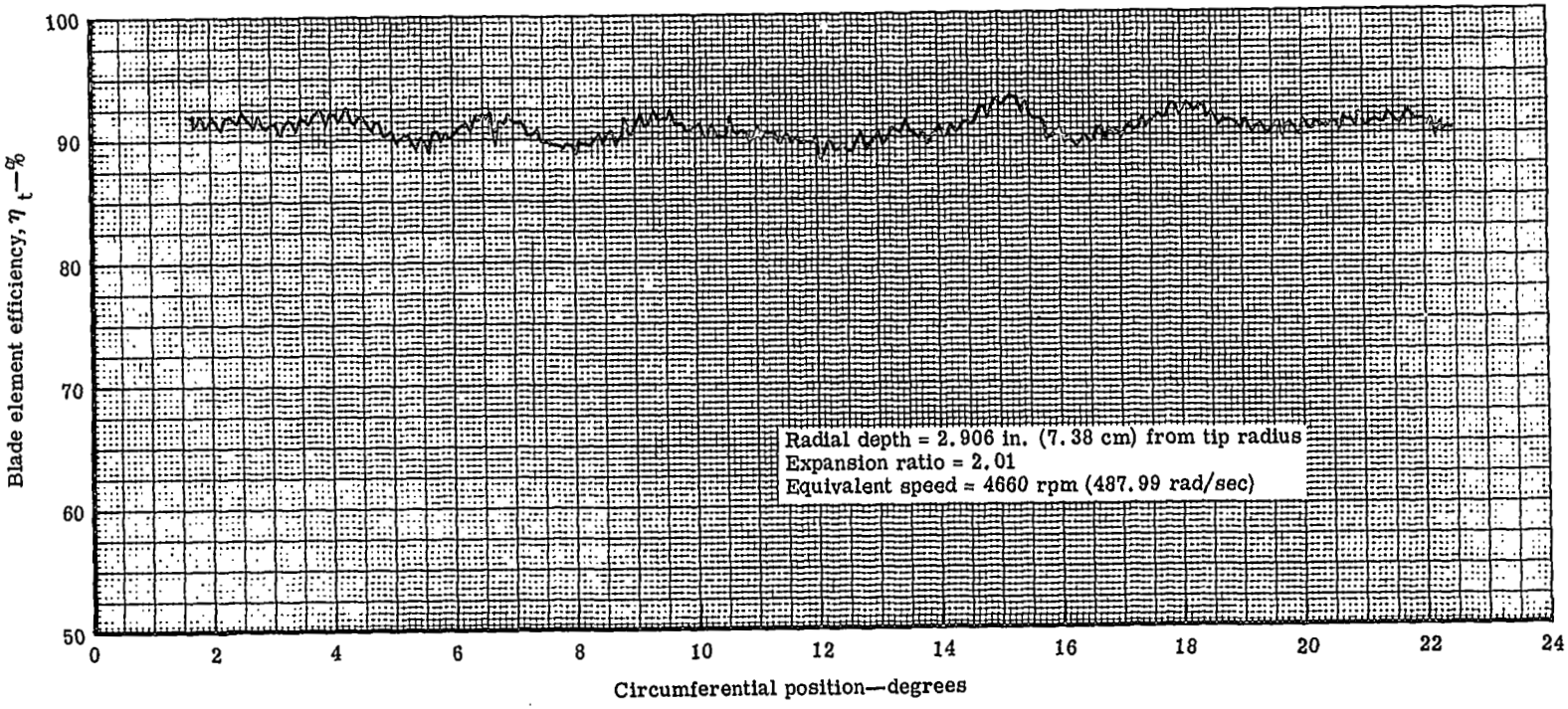

Figure 28. Circumferential variation of blade element total efficiency at rotor exit.

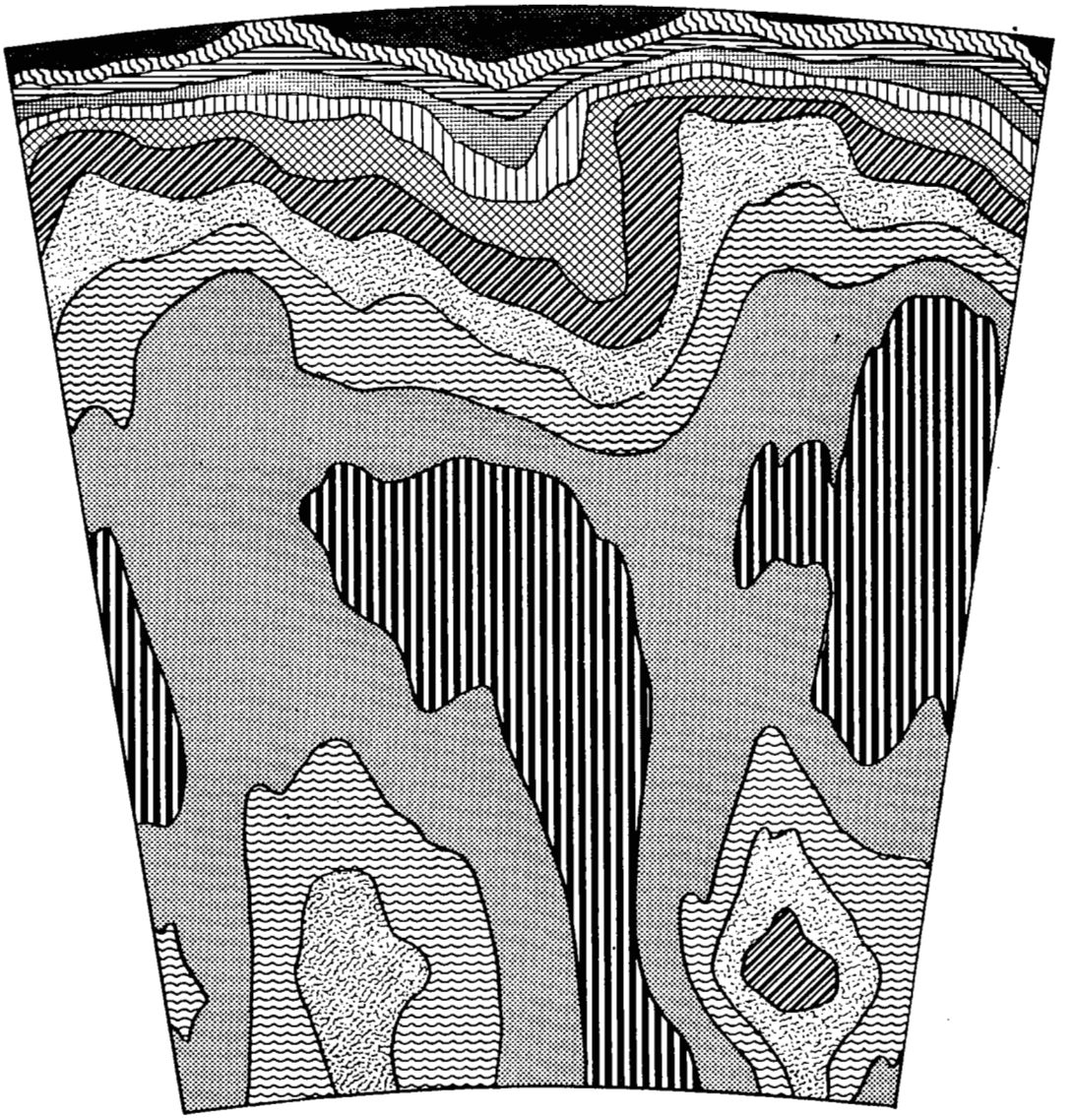

Figure 29. Turbine stage total temperature ratio contours for low solidity tandem rotor blade turbine.

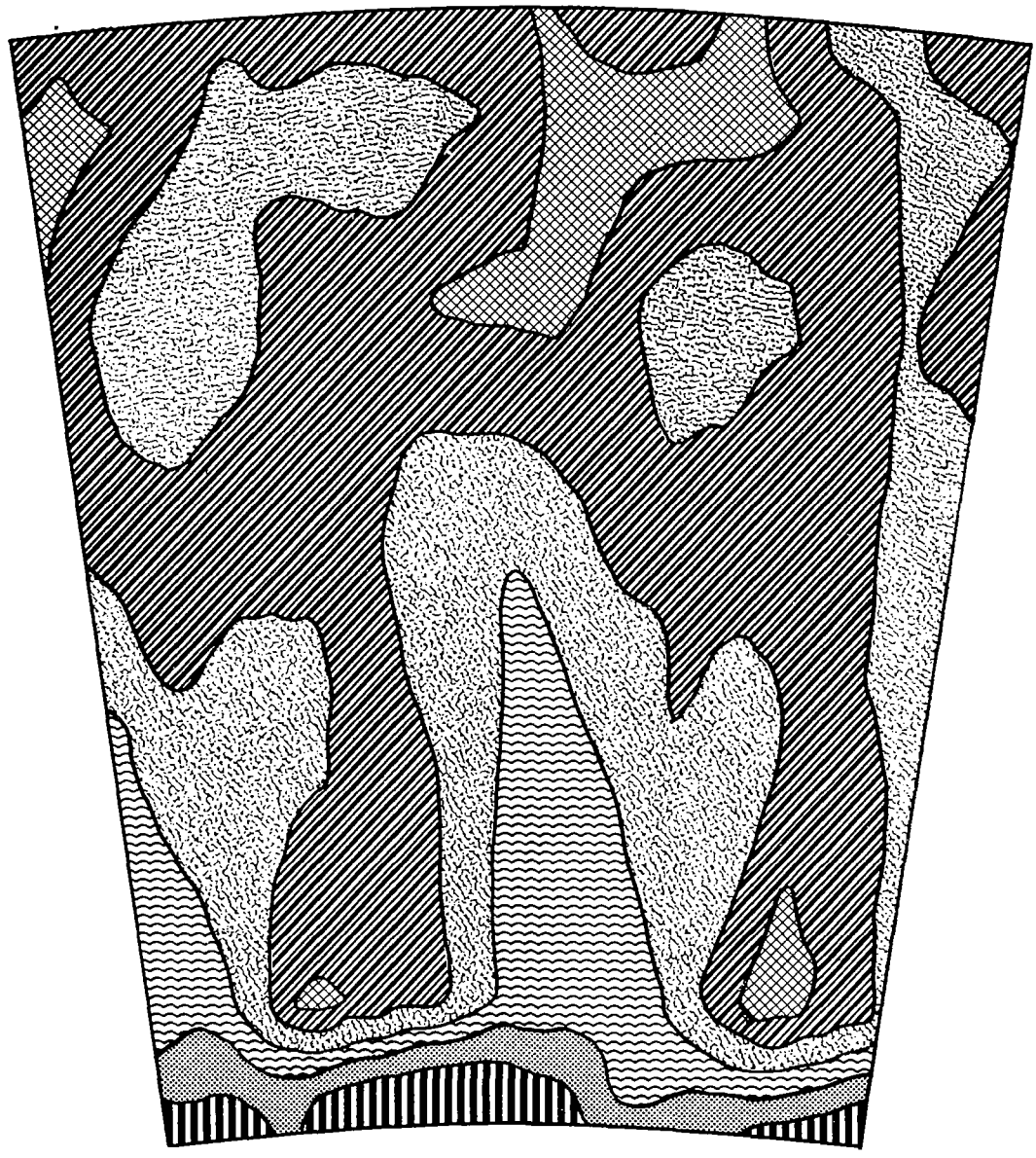

Viewed looking upstream, $N/\sqrt{\theta}_{cr}$ = 4660 rpm (487.99 rad/sec), P_{T_O}/P_{T3} = 2.01

Total pressure ratio, P_{T_O}/P_{T2}

- 2.15 and above
- 2.10 to 2.15
- 2.05 to 2.10
- 2.00 to 2.05
- 1.95 to 2.00
- Below 1.95

Figure 30. Turbine stage total pressure ratio contours for low solidity tandem rotor blade turbine.

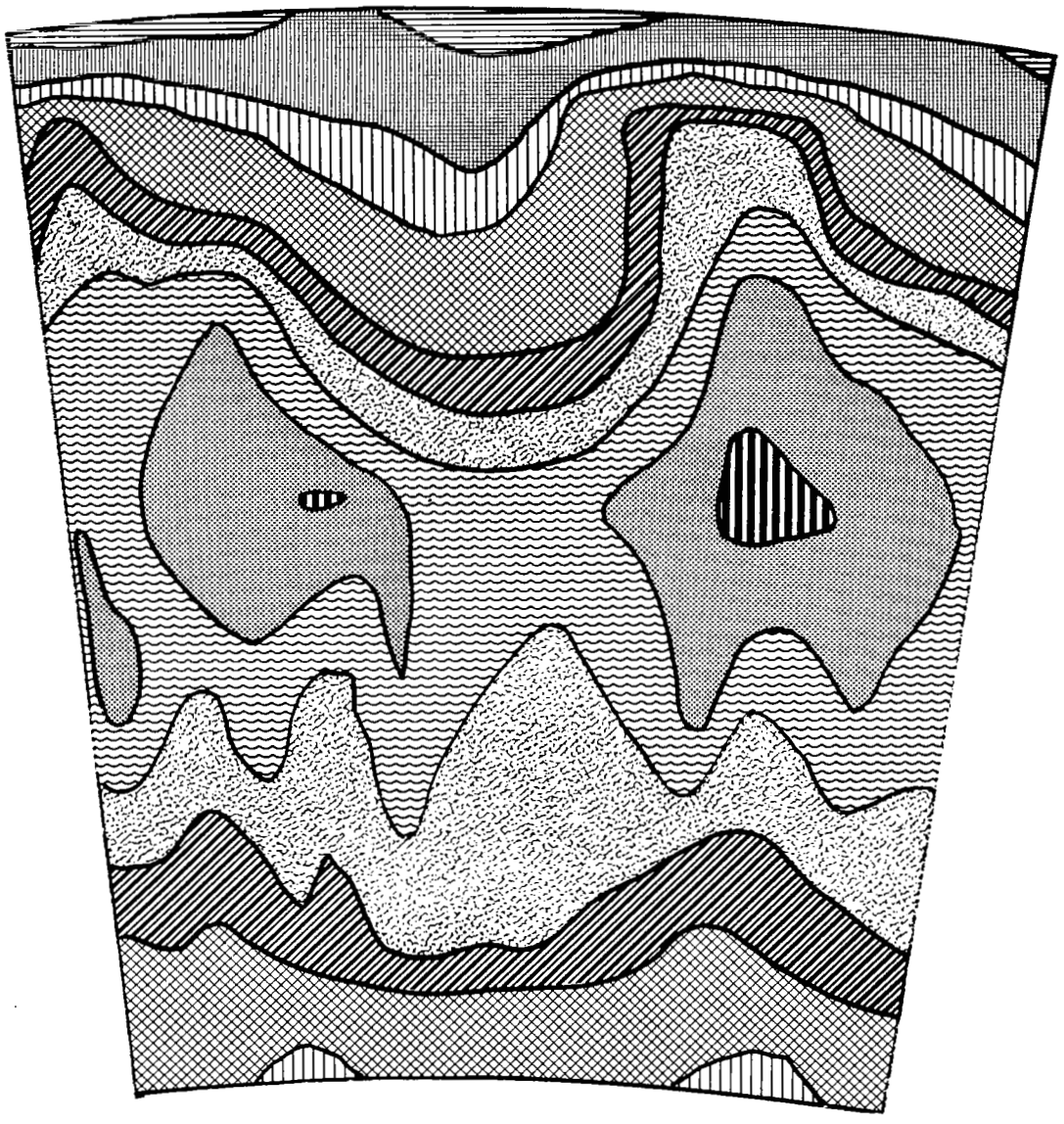

Viewed looking upstream, $N/\sqrt{\theta}_{cr}$ = 4660 rpm (487.88 rad/sec), P_{To}/P_{T3} = 2.011

Total-to-total efficiency, η_t

- 0.94 and above
- 0.92 to 0.94
- 0.90 to 0.92
- 0.88 to 0.90
- 0.86 to 0.88
- 0.80 to 0.86
- 0.76 to 0.80
- 0.68 to 0.76
- Below 0.68

Figure 31. Turbine stage total efficiency contours for low solidity tandem rotor blade turbine.

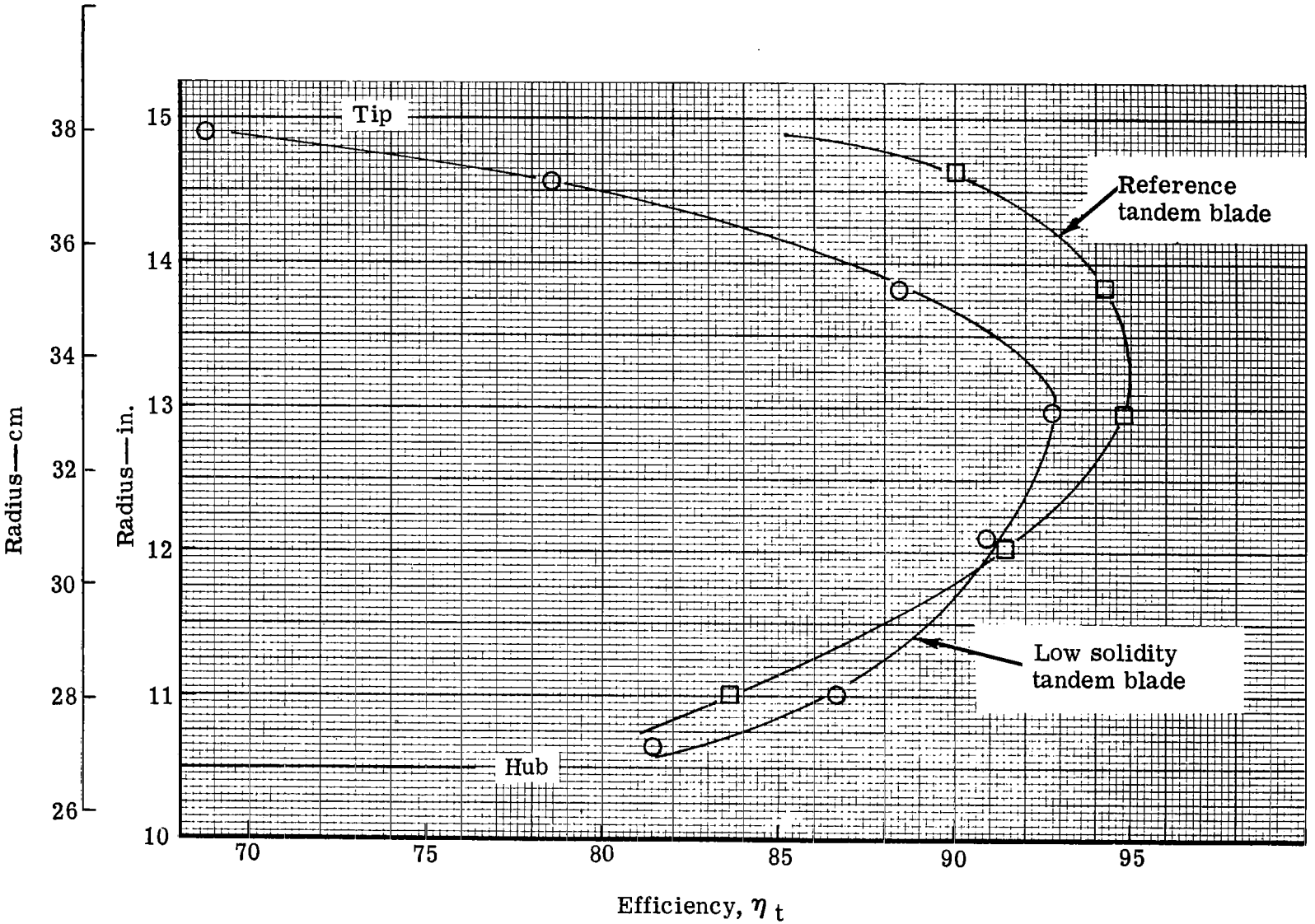

Figure 32. Comparison of radial distribution of stage efficiency for the modified and low solidity tandem blade turbines.

NASA-Langley, 1971 — 1